Cloud Climatology and Microphysics at Eureka Using Synergetic Radar/Lidar Measurements

Jasmine Rémillard

Master of Science

Department of Atmospheric and Oceanic Sciences

McGill University

Montréal, Québec

August 2008

A thesis submitted to McGill University in partial fulfillment of the requirements of the degree of Master of Science.

ACKNOWLEDGEMENTS

I would like to thank my supervisor, professor Pavlos Kollias, without whom this project wouldn't have been possible. His expertise and acquaintance with other researchers in the cloud remote sensing community were very helpful. Through enlightening discussions and stimulating ideas, this project was a great experience and a success. Many thanks go to all the other members of the radar group, especially professors Isztar Zawadzki and Frédéric Fabry, for their comments and support throughout the project.

Special thanks go to Matthew Shupe, from the NOAA ESRL, and Edwin Eloranta, from the University of Wisconsin, for providing the MMCR and AHSRL data, respectively, and for their enthousiasm about the project and its results. Further thanks go to Ed Hudson, from EC, for his eagerness to help us with the HRPT images and other Arctic matters.

Discussions and comments from attendees of the AMS annual meeting, the AOS student seminars and the pan-GCSS polar clouds working group were also greatly appreciated. Finally, the unconditional encouragement from my family throughout these many years of study was very helpful.

Funding was provided by the Natural Sciences and Engineering Research Council of Canada, the government of Quebec, the department of Atmospheric and Oceanic Sciences, and McGill University.

ABSTRACT

Despite their importance in Earth's radiation budget and atmospheric models, Arctic clouds remain poorly documented and understood. The deployment of a cloud radar and a high spectral resolution lidar at Eureka (80°N) in August 2005 offers a unique data set for the study of Arctic clouds. In this project, synergetic retrievals were developed and applied to two years of data in order to provide a first climatology of the clouds and their microphysics at this remote location. Results show an annual cycle in cloud coverage. They are mostly detected in the low levels or in single-layer, especially in winter due to a temperature inversion and cloud top radiative cooling. An analysis of the winds also demonstrated that different wind directions relate to different cloudiness conditions, while a strong channelling from the topography is present in the low levels. Moreover, liquid phase particles were detected all year round, with a minimum occurrence in winter due to colder temperatures. Turbulence and high relative humidity seem to maintain supercooled liquid, especially when ice crystals were also present. Precipitation was mostly identified during summer months, often in the form of virga, although falling snow might have been missed due to the difficulty to distinguish it from glaciated clouds. Finally, results show that satellite validation is possible using Eureka's data, but only under homogeneous conditions and when the instruments characteristics (like the sampling and sensitivity) are taken into account.

ABRÉGÉ

Malgré leur importance dans le budget radiatif terrestre et les modèles atmosphériques, les nuages arctiques restent mal documentés et incompris. Le déploiement d'un radar millimétrique et d'un lidar à haute résolution spectrale à Eureka (80°N) en août 2005 offre un ensemble unique de données pour l'étude des nuages arctiques. Dans ce projet, des algorithmes synergétiques furent développés et appliqués à deux ans de données pour fournir une première climatologie des nuages et de leur microphysique à cet emplacement éloigné. Les résultats montrent un cycle annuel dans l'étendue des nuages. Ils sont surtout détectés dans les bas niveaux ou en une couche, particulièrement en hiver à cause de l'inversion thermique et du refroidissement radiatif du haut des nuages. Une analyse des vents a démontré que différentes directions sont reliées à différentes conditions nuageuses, alors qu'une forte canalisation des vents due à la topographie est présente dans les bas niveaux. De plus, la phase liquide fut détectée à l'année longue, avec une occurrence minimale en hiver causée par des températures plus froides. De la turbulence et un haut taux d'humidité semblent maintenir les particules liquides surfondues, particulièrement quand des cristaux de glace sont aussi présents. Les précipitations furent principalement identifiées durant l'été, surtout sous forme de virga, bien que la difficulté à distinguer la neige des nuages glacés a pu influencer les résultats. Finalement, la validation d'un satellite est possible grâce aux données d'Eureka, mais seulement sous des conditions homogènes et si les caractéristiques instrumentales (telles que le prélèvement de données et la sensibilité) sont considérées.

TABLE OF CONTENTS

LIST OF TABLES

LIST OF FIGURES

Chapter 1
Introduction

1.1 "The Cloud Problem"

Clouds play a critical role in Earth's climate system. Their participation to Earth's hydrological cycle[1] starts with their formation through the condensation of atmospheric water vapor into small droplets and ice crystals, their subsequent growth and partial or total evaporation (or melt and sublimation for snow), as they drift and fall. Moreover, precipitation originates from clouds.

Clouds are responsible for most of the three-dimensional heat and moisture redistribution (Gulteppe et al., 2000). Throughout their life cycle, clouds exchange heat with the environment: the condensation of water vapor releases latent heat and warms the surrounding air, while heat is required to evaporate water drops and melt/sublimate ice crystals, thus cooling the environment. These processes occur at different atmospheric levels. Consequently, a net vertical heat transport is obtained. Furthermore, their timing differs: the former process arises mostly at the beginning of a cloud's life, while the later happens mostly towards the end of it. So, as the

[1] The *hydrological cycle* is the name given to the circulation of water in any phase (vapor, liquid and solid) between land, ocean and atmosphere, by processes such as condensation, precipitation, infiltration, runoff and evaporation.

cloud drifts with the main atmospheric currents, a net horizontal heat and moisture redistribution also occurs.

Finally, clouds are a dominant factor in Earth's radiation budget, through their interactions with radiation. Clouds reflect and absorb a fraction of the Sun's (shortwave) radiation, while they absorb and emit terrestrial (longwave) radiation. This results in either a warming or a cooling of the Earth's system. As clouds block a fraction of the incoming solar radiation, they cool the atmosphere. Clouds also trap longwave radiation and, as a result, warm the atmosphere. Overall, clouds have a strong cooling effect on the Earth's system (Harrison et al., 1990; Ramanathan et al., 1989).

Despite their importance and ever increasing computational power and model sophistication, cloud processes are poorly represented in numerical models. This constitutes one of the major sources of uncertainty in numerical simulations of climate and weather. For instance, Cess et al. (1995) showed that the models significantly underestimate the absorption of solar radiation by clouds. Later, Rinke et al. (1997) improved their modeled results through a better parameterization of the atmospheric absorption, although the agreement was still unsatisfactory. Moreover, Bony and Dufresne (2005) suggested that the models are not accurately simulating the sensitivity of the marine boundary layer clouds to changes in the sea surface temperature, primarily in the tropical regions, and Randall et al. (1998) indicated the need to use a better parameterization of the interactions between the ocean, ice and atmosphere in the Arctic for any large-scale modeling.

Clouds propensity for precipitation and their radiative properties are highly dependent on their macrophysical and microphysical properties. For example, deep cumulus clouds contain large precipitation-size particles and have large optical depth, thus effectively blocking solar radiation. On the other hand, deep cumulus are also effective in trapping Earth's emitted thermal radiation (Pinto et al., 1997). The cloud altitude influences as much through changes in the relative amount of each type of received radiation (mainly a change in the infrared part as the air absorbs it too) and in the temperature of the particles relative to the surface (Atlas et al., 1995). For instance, a cloud will trap less longwave radiation if its base is higher, thus reducing the warming of the surface (Pinto et al., 1997). In addition, the solar zenith angle (determined by the latitude and the time) also influences the interactions: a greater angle usually means more reflection, while the effect on the absorption depends on the phase of the water in the clouds (Sun and Shine, 1994).

The situation gets even more complex when accounting for overlapping cloud layers. For example, there could be a cirrus cloud over a boundary layer cloud. This is called a *multi-layer* system, as opposed to a *single-layer* one. The total effect of the system is not a simple sum of the effect of each cloud forming it. Although each cloud layer will reflect and absorb the same fraction of received radiation as in a single-layer case, some of it could get trapped in the atmosphere between the cloud layers.

Finally, the life cycles and radiative properties of clouds are highly sensitive to the phase (liquid or ice), size and shape of their hydrometeors. For instance, although the reflectivity and absorption increase with the amount of water of any

phase, it is more important for liquid droplets than crystals, especially at low water content (Harrington and Olsson, 2001; Sun and Shine, 1994). The only exception happens for the absorption at high solar zenith angle, as it increases if the particles are solid and decreases if they are liquid. The phase also has an indirect effect on the radiative properties of a cloud, as the liquid hydrometeors are usually smaller, denser and more numerous then their solid counterpart (Shupe and Intrieri, 2004).

As for the size of the hydrometeors, simulations seem to show that an increase in the effective radius of liquid drops increases the amount of shortwave radiation received at the surface and decreases the longwave amount, while the opposite applies for a decrease in effective radius (Curry and Ebert, 1992). On the contrary, larger crystals seem to increase the longwave radiation of the cloud, warming the surface more, while decreasing its shortwave absorption (Harrington and Olsson, 2001). The shape of the crystals can also influence the net radiative effect of an ice cloud, as a dendrite has more branches to interact with radiation than a column for example, especially when the ice water content is large (Harrington and Olsson, 2001; Wendisch et al., 2005).

Based on those differences, modeling studies have shown that the distribution of both phases must be represented in the simulations to get more accurate results. Misrepresentation of cloud radiative properties in numerical models can result in large errors in the calculation of cloud radiative fluxes, which are required to simulate the present-day (Gregory and Morris, 1996) and future (Sun and Shine, 1995) climates. In fact, Ho et al. (1998) indicated that the inclusion of the ice phase decreases the global absorption of shortwave radiation. Moreover, Vavrus (2004) suggested that the

ice phase presence might be responsible for the smaller cloudiness during the winter season, as it has a shorter residence time in clouds than its liquid counterpart.

As Shupe et al. (2006) suggested, this is particularly true in high latitudes, where the temperatures persist most of the year between −40 and 0℃. It is only in those conditions that both hydrometeor phases are sustainable: above the freezing level, any ice particle will melt and turn into liquid, while below −40℃, any liquid will homogeneously nucleate and solidify. But, between those limits, both phases can coexist. The liquid part is then said to be *supercooled* and the clouds containing liquid and ice particles at the same time are called *mixed-phase* clouds. Their radiative properties are highly dependent on the actual temperature and the amount of supercooled liquid, and they are different than other clouds. Those clouds then need to be accounted for in the models, at all levels (Sun and Shine, 1994) and all latitudes (Tsushima et al., 2006).

As suggested by Senior and Mitchell (1993), climatologies of cloud occurrence, vertical extent, altitude, hydrometeor phase and size for different locations can help reduce the model uncertainties, through an assessment of their current effect on Earth's climate and prediction of their future contribution to Earth's radiation budget. To do so, millimeter-wavelength radars (radars sensitive to small cloud droplets, also called cloud radars) and lidars (as a radar, but using a wavelength in the light range) can be of great help, as they are capable of resolving with good accuracy the vertical distribution of cloud layers and can be used to produce a cloud type climatology with vertical layering information (Clothiaux et al., 2000). In addition,

synergetic measurements from cloud radars and lidars have been used in the past to infer hydrometeor type and phase (e.g., Shupe, 2007; Shupe et al., 2006).

1.2 Importance of Arctic Clouds

Model simulations (Shupe and Intrieri, 2004; Sun and Shine, 1994, 1995) suggest that cloud liquid water content (LWC) has a huge impact on the clouds radiative properties, even in small amounts. Recent field studies (such as the Surface Heat Budget of the Arctic Ocean (SHEBA) Program (Intrieri et al., 2002; Shupe et al., 2006) and others (Curry et al., 1997; Pinto, 1998; Rangno and Hobbs, 1991)) have demonstrated that the Arctic clouds contain liquid all-year round, even during the winter season.

In the Arctic, clouds play an important role on the sea-ice extent and thickness through their contribution to the surface radiation budget. During the winter, when the solar rays do not reach the Arctic, clouds reduce the cooling of the surface, by trapping a part of its outgoing radiation. On the contrary, during the summer, when the sun is always shining on the Arctic, it is the clouds presence that prevents some of the radiation from reaching the surface, thus slowing down its warming. In fact, Curry and Ebert (1992) demonstrated that the clouds are warming the Arctic surface most of the time. The only exception was found during a short period of the summer season.

Consequently, changes in polar cloudiness can affect the climate of the whole planet. For instance, the midlatitude winter weather is drastically influenced by the Arctic cold air (Randall et al., 1998). Moreover, Sokolova et al. (2007) showed that the Northern Hemisphere storm tracks are influenced by the extent of the sea ice

covering the Arctic Ocean through a modulation of the sub-polar westerlies strength and of the quasi-stationnary planetary waves. Furthermore, the polar climates are the most sensitive on Earth to any change, due to their cold and dry atmosphere (Shupe et al., 2006).

However, the observations available from the Arctic, when they do exist, are quite sparse. They come from local inhabitants, ships drifting in the ocean (first one in 1893-96), Russian drifting ice camps (until 1991), and recent field experiments (ground-based or from aircrafts). This sparsity of the record is due to the fact that the environment is quite harsh. Consequently, not many people inhabit the Arctic regions, and any observation log kept on those regions will be, at best, localized to places where humans happen to live at that moment. Moreover, during the winter season, the darkness prevents any observations from being accurate and precise, although the moonlight can help when some criteria are filled (see Hahn et al., 1995, for more information). Furthermore, unlike the Antarctic region, the Arctic is mainly made of an ocean partly covered by ice, which extent varies. Consequently, only some regions are easily accessible all-year round, which complicates things for a global Arctic analysis based on ground measurements. Finally, the data collection is not necessarily profitable in most of the Arctic, and the need for better observations was not fully understood until recently.

Therefore, the satellites might seem to be a better solution for the characterization of the Arctic atmosphere. Since the Earth's curvature prevents geostationary satellites from being used, it would have to be a polar orbiting one, which happens to pass near the poles often (depending on the orbit), providing a good coverage of

them, even though they never pass over them directly. In fact, they have been used by Wang and Key (2003) to show that, over the past two decades, the cloud cover has already started to increase during the summer and spring seasons, while it has decreased for the winter, consistent with the observed warming of the Arctic during the summer and cooling over the winter.

However, this method requires careful adjustments in order to be used over the poles, as it is hard to distinguish well the clouds from the surface, in both visible and infrared channels (Lubin and Morrow, 1998). When the former is available (during the whole summer but never in the winter), snow and ice covers are easily mistaken for clouds (see figure 1–1a). In the infrared images (based on the radiation, which is a measure of the temperature), the low clouds signal can be mistaken for the surface (see figure 1–1b), as their temperatures will be rather close. Moreover, the cold snow and ice often produce a characteristic temperature and humidity inversion near the surface (Lubin and Morrow, 1998). Consequently, the clouds might even be warmer than the surface (Randall et al., 1998). Finally, the cold temperatures of a polar atmosphere allow it to emit only small amounts of longwave radiation (Lubin and Morrow, 1998).

Moreover, many studies (Curry and Ebert, 1992; Intrieri et al., 2002; Rinke et al., 1997) have shown that the boundary layer clouds are an important type in the Arctic, prevailing all year long. And despite some progress made in the detection of nighttime clouds from satellites (Liu et al., 2004), the retrievals of cloud overlap, cloud phase and hydrometeor size from space remain a challenge, especially in the Arctic. Thus, the satellite's instruments would have to be able to penetrate the

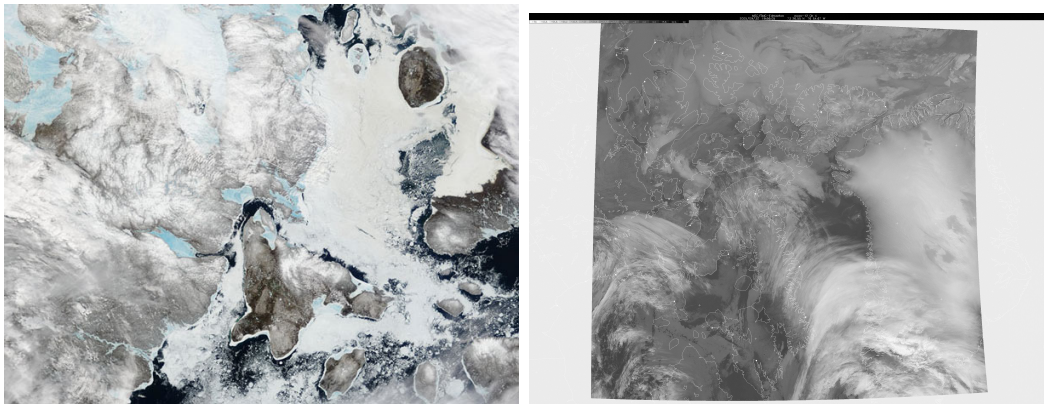

Figure 1–1: Satellite pictures of the Arctic taken in the visible by a NASA's MODIS (left, courtesy of J. Descloitres from the MODIS Land Rapid Response Team), representing the Foxe Basin on June 20, 2002, and in the infrared by the NOAA's HRPT (right, courtesy of E. Hudson from Environment Canada), representing the Canadian Arctic on September 30, 2005.

clouds and give some vertical profiles of the troposphere, but the coverage will stay sparse, as no satellite can be observing a polar region continuously. Nevertheless, their data would be relevant to validate any results obtained from a ground-based station, to verify their application to a larger scale.

1.2.1 CANDAC Facilities at Eureka

The Canadian Network for the Detection of Atmospheric Change (CANDAC, www.candac.ca) was created in 2002 from a consortium of Canadian universities with the goal to improve the state of observational atmosphere research in Canada. As a result, CANDAC established in 2002 a permanent atmospheric observatory in the Arctic, the Polar Environment Atmospheric Research Laboratory (PEARL), in a formerly existing housing. The Meteorological Service of Canada (MSC) had it built on a ridge of about 610 m, 15 km upwind from Eureka, a remote weather station located near the Arctic Circle (79°59′25″N, 86°56′20″W) in a bay of the Ellesmere

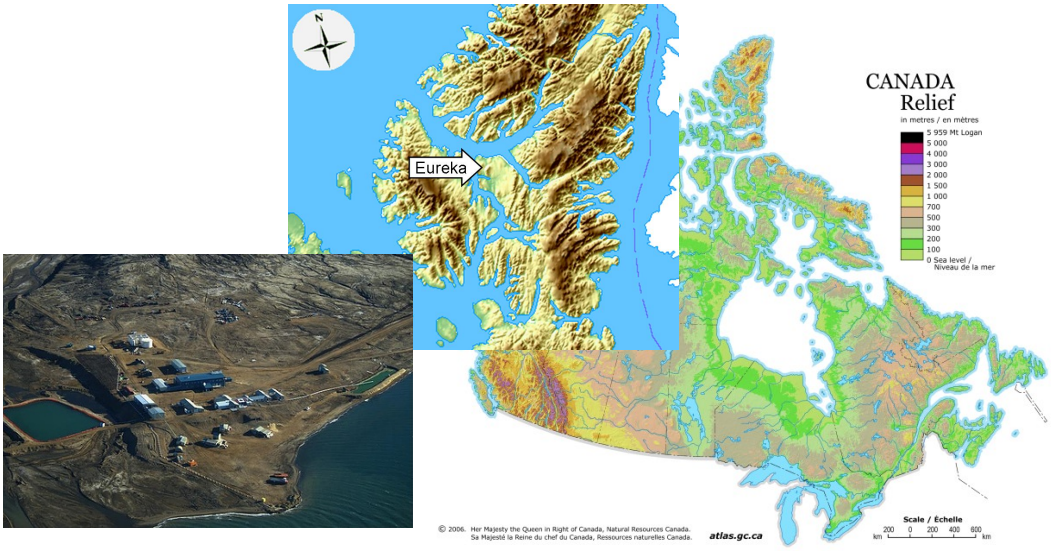

Figure 1–2: Topographic map of Canada, with an enlargement of most of the Ellesmere and surroundings islands (courtesy of Natural Resources Canada). The arrow points to Eureka's location, while the insert shows an aerial view of the weather station (courtesy of P. Fogal from CANDAC).

Island (Nunavut, Canada, see figure 1–2). This location was chosen to ensure an uncontaminated air mass in their study of the stratospheric ozone. Fortunately for CANDAC, the MSC research ended in the summer of 2002, vacating the building.

In 2005, a second laboratory was established in the North-West quadrant of Eureka, the Zero Altitude PEARL Auxiliary Laboratory (ØPAL), to study the vertical structure of the clouds, precipitation and aerosols. And now, CANDAC is building the Surface and Atmospheric Flux, Irradiance and Radiation Extension (SAFIRE) on a undisturbed terrain five kilometers away from Eureka, to better understand the radiation budget of that Arctic region. Figure 1–3 shows pictures of each of the CANDAC's facilities.

Figure 1–3: The three laboratories of the CANDAC: PEARL on the left, ØPAL in the center and SAFIRE on the right (courtesy of P. Loewen from CANDAC).

The primary purpose of those three facilities is to study the Eureka atmosphere from the surface to 100 km, over a continuous and prolonged period of time, to assess its current state and be able to detect future changes, as well as to try to answer some current atmospheric science questions. To achieve it, a wide variety of instruments (such as spectrometers, radars, lidars and photometers) are operating at the Eureka site, with some of them collecting continuous data since 2005. Both optical remote sensing and *in situ* sampling are supported by the facilities, which makes them an ideal place to study global atmospheric change and to validate satellites atmospheric measurements.

More specifically, the ØPAL facility includes the Millimeter Wave Cloud Radar (MMCR) co-located with the Arctic High Spectral Resolution Lidar (AHSRL), both provided by the US National Oceanic and Atmospheric Administration (NOAA) Study of Environmental Arctic Change (SEARCH) program. Each of them occupies half of the light blue sea-container (the second from the left in the center panel of figure 1–3, with the radar being the closest from this view, under the antenna that clearly shows on the roof). This combination of highly sensitive instruments is unique

to Eureka and is operating since August 12, 2005 in an unattended and automated manner.

1.3 Research Objectives

The project's main objective is to characterize clouds and precipitation occurrences at Eureka over a long period (two years, September 2005 to August 2007), using combined measurements from the MMCR and AHSRL. The cloud and precipitation signals are differentiated from each other and from aerosols, to produce a realistic climatology of the clouds properties, such as their occurrence, height, depth and precipitation. Daily and monthly averages of those quantities are computed to get an idea of their annual and seasonal cycle. Furthermore, the hydrometeors (cloud and precipitation particles) are classified according to their phase (ice, liquid or mixed). The results are then related to the synoptic and dynamic situations.

The present thesis is organized such that a complete description of the two instruments of interest (MMCR and AHSRL) is first given in chapter 2, along with some samples of the measurements and their interpretation, on their own and combined together. Then, the methodology used to do the different classifications is described thoroughly in chapter 3, while the results are given and discussed in chapter 4. The utility of the measurements and results from those instruments for sensors onboard satellites is evaluated in chapter 5. Finally, some conclusions are drawn in chapter 6, with future work that needs to be carried out.

Chapter 2
Instrumentation

Due to their importance, clouds have been studied for decades, using a wide spectrum of sophisticated instruments. These sensors can be grouped in two categories according to their distance from the object they want to measure: the *in situ* instruments (such as rawinsondes and aircraft microphysical probes), which take measurements of their close surrounding area, and the *remote sensors* (such as radars), that are looking at clouds from a distant location, either by scanning the atmosphere in two or three dimensions or always looking at the same column of the atmosphere (usually vertically pointing). Furthermore, cloud observations are classified with respect to the platform used: i) *ground-based* if the instrument is located on the ground (or close to it), either at a permanent or mobile site, ii) *airborne/ship-based* if it is operated from an aircraft or a ship, and iii) *space-borne* if it is onboard a satellite.

Each measurement approach has advantages and disadvantages. For instance, space-borne instruments allow a global view of clouds and precipitation, including over the oceans and "hard-to-access" environments (as the Arctic). However, the measurements at a particular location have coarse spatial and temporal resolution. On the contrary, ground-based instruments provide continuous data sets with high resolution, but only for its given location and the surrounding areas. Thus, a big number of such ground-based stations are required in order to put together a global

view of clouds, precipitation and aerosols, with ship-based instruments needed to observe the oceanic atmosphere (providing only discontinuous data record, biased along the ships' paths). Finally, the data taken from an aircraft will be discontinuous, as the aircraft cannot fly indefinitely over a given region. Ultimately, the choice depends on the scientific goals of the research: here, getting a climatology of the clouds behavior in the Arctic is the main objective.

Remote sensors are further divided in two categories: *passive* (such as microwave radiometers), which simply detects radiation emitted toward its antenna by the atmosphere, the particulate matter (aerosols and hydrometeors) and the sun, and *active* (such as radars and lidars), which sends a signal at a given frequency for a short time duration and analyzes the part of the transmitted energy that is scattered back to the instrument from the atmospheric molecules and particulate (also called the *echo* of the signal). Active sensors are capable of making range-resolved measurements, contrary to passive instruments that detect integrated signal along their line of sight.

Since various wavelengths are available, the choice is mainly based on the research goals. A passive instrument will use those close to an absorption peak of the desired atmospheric part. Thus, a radiometer observing the atmospheric water vapor will choose frequencies around 22 GHz or 183 GHz, depending on the expected amount, while someone interested in the atmospheric oxygen (and thus, temperature profiling) will prefer frequencies around 60 GHz. On the contrary, a frequency from an atmospheric window is used by an active sensor, with the actual choice based on the primary goal, as described by Moran et al. (1998). For instance, meter-wave signals can simply resolve wind patterns (hence, used for wind

profilers), while centimeter-wave signals easily detect precipitation (hence, used in weather surveillance radars) and millimeter-wave signals are also sensitive to the cloud particles (hence, used in cloud radars). Finally, lidars use lasers to produce their signals, which are in fact light beams. Consequently, their wavelengths range from 250 nm to 11 μm, respectively in the ultraviolet and near infrared regions of the electromagnetic spectrum (Wandinger, 2005).

In order to get additional information on the observed atmosphere, further characteristics can be added to the remote sensors, such as Doppler and polarization capabilities, providing information about, respectively, the motion and the non-sphericity of the targets. Nevertheless, it is usually better to use instrument combinations (called a *synergy*) to better characterize the sampled area. The suitable combination of active and passive sensors depends on the research objectives. At Eureka, as in many cloud studies, a Doppler cloud radar and a depolarization lidar are employed, since their observations complement each other: the radar signal is dominated by the ice crystals, while the lidar detects cloud droplets (see sections 2.1.1 and 2.2.1, respectively). Only rawinsondes data are added to refine the phase characterization aspect, although it is widely accepted (see the US Department of Energy's Atmospheric Radiation Measurements (ARM) Program (Ackerman and Stokes, 2003, www.arm.gov) and the European Cloudnet project (Illingworth et al., 2007, www.cloud-net.org)) that a two-channel microwave radiometer should be used in such a study, as it indicates the amount of liquid in the whole column.

Over the years, several studies of cloud microphysical and macrophysical properties have been conducted. Most of them used a combination of a cloud radar and

a lidar (like Clothiaux et al., 2000; Tinel et al., 2005; Wang and Sassen, 2002), while some added radiometer measurements (like Illingworth et al., 2007; Shupe et al., 2008a,b) or *in situ* data (as Basedi et al., 2000) and others simply replaced the lidar with a radiometer (as Kollias et al., 2007) or a wind profiler (as Kollias et al., 2001). The vast majority used their instruments on the same platform (all ground-based (as Platt et al., 1999), all airborne (as Tinel et al., 2005) or all space-borne (as Schwartz and Haar, 2008)), and only a few combined different views (as Quante et al., 2000).

Those previous studies were conducted all over the globe, virtually covering all possible climates (tropical, subtropical, mid-latitude and polar, as well as marine and continental) and all heights (high-, mid- and low-level). However, only a few have focussed on the Arctic clouds, and preferably around the North Slope of Alaska (NSA), due to the presence of two sites of the ARM program: one near the Arctic Ocean coast at Barrow (71.32°N;156.62°W) and the other inland at Atqasuk (70.47°N;157.41°W), 110 km South of Barrow. Those research facilities include atmospheric instruments continuously collecting data since their establishment in 1997, and support field studies, such as SHEBA in 1997-98 (Uttal et al., 2002) and the Mixed-Phase Arctic Cloud Experiment (M-PACE) in 2004 (Verlinde et al., 2007).

In August 2005, the CANDAC Eureka site has also been equipped with cloud instruments (see section 1.2.1), but the first analysis of their data is done here. Recently, Russia joined the effort to develop systematic measurements of cloud, aerosol and radiation in the Arctic: the Russian Federal Service for Hydrometeorology and Environmental Monitoring (Roshydromet) replaced their weather station at Tiksi (71.6°N;128.90°E) in 2006 and built another Arctic facility for atmospheric research in

2007, 1.5 km to the North-West of Tiksi, on a quasi-flat area. Although other sites exist around the Arctic, such as in Summit (Greenland, Denmark, at 72.60°N;28.40°W) and Ny-Ålesund (Svalbard, Norway, at 78.96°N;11.90°E), none has any instruments sensitive enough to study clouds. Nevertheless, the NSA, Eureka and Tiksi sites will provide a network of Arctic clouds observations covering various latitudes and longitudes of the Arctic region. In this project, the Eureka data set is used, in order to provide a first analysis of it. Thus, a description of the main cloud instrumentation of the ØPAL facility (the MMCR and AHSRL) follows to help understand their choice and usefulness, as well as the cloud characterizations aspects attempted here.

2.1 Millimeter Wave Cloud Radar (MMCR)

The MMCR design was developed by NOAA's Environmental Technology Laboratory (ETL), on the ARM Program request, to get detailed and precise vertical profiles of the non- or weakly precipitating clouds on a long-term basis (Clothiaux et al., 2000, 1999; Kollias et al., 2007; Martner et al., 2002; Moran et al., 1998).

2.1.1 Technical Characteristics

The primary characteristics of the MMCR hardware are summarized in the first few lines of table 2–1, with the principal being the operating wavelength of 8.66 mm (or frequency of 34.86 GHz, thus in the K_a band). The radar wavelength is much larger than most of the cloud particles (typically 10 μm in diameter), and even drizzle drops (less than half a millimiter in diameter). Consequently, the MMCR operates in the Rayleigh scattering regime in those situations, and the returned signal will be proportional to the number of particles and to the sixth power of the particle size ($N(D)D^6$). Therefore, although the small particles are much more numerous than

Table 2–1: List of the technical characteristics of the four modes of the SEARCH's MMCR during its operations at the Eureka site (based on the settings used by the ARM program at the NSA site: Clothiaux et al., 1999; Kollias et al., 2007; Moran et al., 1998).

Frequency/Wavelength	—— 34.86 GHz/8.66 mm (K_a band) ——			
Peak/Average power	—— 100 W/25 W ——			
Beamwidth	—— 0.3°, circular ——			
Antenna diameter	—— 1.8 m ——			
On-axis gain	—— 57.2 dB ——			
Operating mode	1–stratus	2–general	3–cirrus	4–robust
Interpulse period (μs)	68	96	115	112
Pulse width (ns)	300	600	600	300
Number of coherent averages	6	5	6	2
Number of spectral averages	50	70	23	20
Number of FFT points	256	128	128	128
Number of coded bits	0	0	32	0
Dwell time (s)	1.044	0.983	0.883	0.573
Time resolution (s)	2.1	2.1	2.1	1.7
Range resolution (m)	45	90	90	45
Minimum range (m)	95	95	2975	95
Maximum range (km)	6.125	13.415	13.415	9.995
Unambiguous range (km)	10.20	14.40	17.25	16.80
Nyquist velocity (m/s)	±5.27	±4.48	±3.12	±9.60
Velocity resolution (cm/s)	4.11	7.0	4.87	15.0
Sensitivity (dBZ at 5 km)	−44	−40	−51	−32

the big ones, the latter will dominate the received signal. Thus, the MMCR is more sensitive to the size of the particles than to their number.

The use of millimeter-wavelength radars for cloud research provides some significant advantages (Moran et al., 1998). First, as the strength of a signal echo varies as the invert fourth power of the wavelength in the Rayleigh regime, the system sensitivity to small particles (such as cloud hydrometeors) is greatly increased, easing their detection. Moreover, the short radar wavelength permits the use of a very

narrow beam (0.3° at Eureka) with a small antenna, and a short pulse (less than 1 μs at Eureka), allowing a finer spatial resolution to be achieved along the beam direction (45 to 90 m at Eureka). Consequently, the vertical structure of clouds as they overpass the ground-based site is best resolved.

However, millimeter-wavelength radars also have disadvantages (Moran et al., 1998). The main one is the increased attenuation of the signal by atmospheric gases and liquid water content, limiting their use in a scanning mode. Nevertheless, this does not significantly affect the system at Eureka as it operates in a vertically pointing manner, thus minimizing the extent of the region of interest and the attenuating path (Moran et al., 1998). Moreover, at such a high latitude, the Arctic climate prevents the occurrence of rainfall most of the year, especially the heavy cases (the EC archives show a climate normal of less than 15 mm of rain per month), while restraining the vast majority of clouds to evolve in the first 10 km of the atmosphere.

Additional details of the MMCR hardware design are listed in table 2–1. Its low-peak-power transmitter extends the lifetime of the system and minimizes the need for service in an area that is difficult to access (Moran et al., 1998). Consequently, it can stay unattended for longer time periods, which well suits the Eureka location.

However, some of the operational characteristics of the MMCR bring undesired effects (Clothiaux et al., 2000; Moran et al., 1998). For instance, pulse compression techniques might generate *range sidelobes* (a smearing of echoes), especially near strong echoes, contaminating the surrounding areas, while the low-level echoes are only partially decoded, raising the lowest usable range. To get around those problems, an MMCR cycles through four operating modes, taking advantage of the fact

that different combinations of the operational parameters yield different data characteristics, such as the unambiguous range and velocity, range coverage, resolutions, sensitivity and noise fluctuations. In fact, most settings can be adjusted to fit the environment and user objectives (Moran et al., 1998) and can quickly be changed if the situation requires it, since the MMCR is run remotely (Clothiaux et al., 1999).

The ultimate goal of an MMCR being the depiction of the vertical distribution of clouds in the whole troposphere above it, the different modes are designed such that they have complementary characteristics. Table 2–1 summarizes the settings used at the NSA site, which are also used at Eureka since the environment is quite similar. In fact, each mode is usually used for the same purpose in the different ARM research sites and Clothiaux et al. (2000) described them, based on their basic observational goals and attributes, as follows:

1 the *stratus* mode has high sensitivity and vertical resolution, at the expense of its height coverage, in order to resolve the boundary layer;
2 the *general* mode is set to resolve most clouds present throughout the whole tropospheric column, using a high sensitivity and coarse vertical resolution;
3 the *cirrus* mode has the highest sensitivity and a coarser vertical resolution mainly to detect the weakly reflective and the high clouds;
4 the *robust* mode has the lowest sensitivity, but is virtually free of all artifacts and accuracy limitations and can resolve greater velocities.

2.1.2 Measurements

The MMCR works by sending a signal at a frequency of 34.86 GHz during a short period of time (the pulse width). That beam encounters atmospheric scatterers

(hydrometeors, insects, birds...) and interacts with them through absorption and scattering processes. Only the part scattered at 180° exactly (the backward direction, hence *backscattered* echo) is of interest to the MMCR, as it is the one coming back to its antenna, at the same frequency. If it is strong enough, the radar detects it and its digital signal processor analyzes it. Since it has Doppler capabilities, the full Doppler spectrum is computed at all ranges of each profile. From it, four quantities are computed: the power density spectrum and the first three spectral moments, namely the reflectivity factor (given in dBZ[1] units), Doppler velocity (in m/s) and Doppler spectral width (also in m/s). Those data require less storage space than the full Doppler spectra and are thus stored instead, for future scientific use (Clothiaux et al., 1999).

The radar can resolve echoes starting at 95 m above ground level (AGL), except when pulse-coding compression is used (in cirrus mode), while the maximum range varies between 6 and 14 km, due to different interpulse periods (see table 2–1). However, the maximum range that the MMCR actually resolves is always less than the unambiguous range (see table 2–1), as a compromise between the coverage and the time resolution. Anyway, there should not be clouds forming, or even extending, higher than 13 km in the Arctic troposphere and the processed range of each mode includes the heights where it is most useful. As for the velocity ranges (the *Nyquist* velocities) and resolutions, they also vary between modes (see table 2–1), as they

[1] Like the decibel (dB) unit used to measure sound levels, the dBZ unit represents $10 \log_{10}(value[mm^6/m^3])$, shrinking the spread of the actual values.

mainly depend on how the averaging is handled. It is important to note that the velocity measured is the *Doppler* velocity, which is the summation of the component of the particles fall speed and air motion along the beam path, with positive values indicating a movement toward the radar (thus, downward here).

To use the full potential of an MMCR, the data acquired from a complete cycle are merged together using an algorithm based on the one developed by Clothiaux et al. (2000), implying an interpolation of the data from each mode into a time-height grid that has resolutions of 10 s and 45 m, with the lowest height at 95 m. Taking all measurements at any given grid point from the same mode, the merging tries to maximize the continuity in the resolutions and to use each mode where it is the most useful, while removing artifacts caused by pulse-coding techniques, coherent averaging and second-trip echoes. An example of the final result at Eureka, including the mode used for each volume, is given in figure 2–1 with the case of September 9, 2005. Note that *UTC* stands for Universal Time Coordinates, which is six hours later than the local standard time observed at Eureka. Profiles of the 10-s measurements are also given for two time steps: one in the deep morning echo and the other in the two shallow afternoon layers.

2.1.3 Interpretation

A quick look at the MMCR measurements can already give some informations about the observed region. For instance, if the reflectivity factor is high, the radar is probably aiming at precipitation, as those hydrometeors are usually bigger than any others. High downward Doppler velocity and spectrum width measurements are also characteristics of precipitation. On the contrary, if the reflectivity factor is very

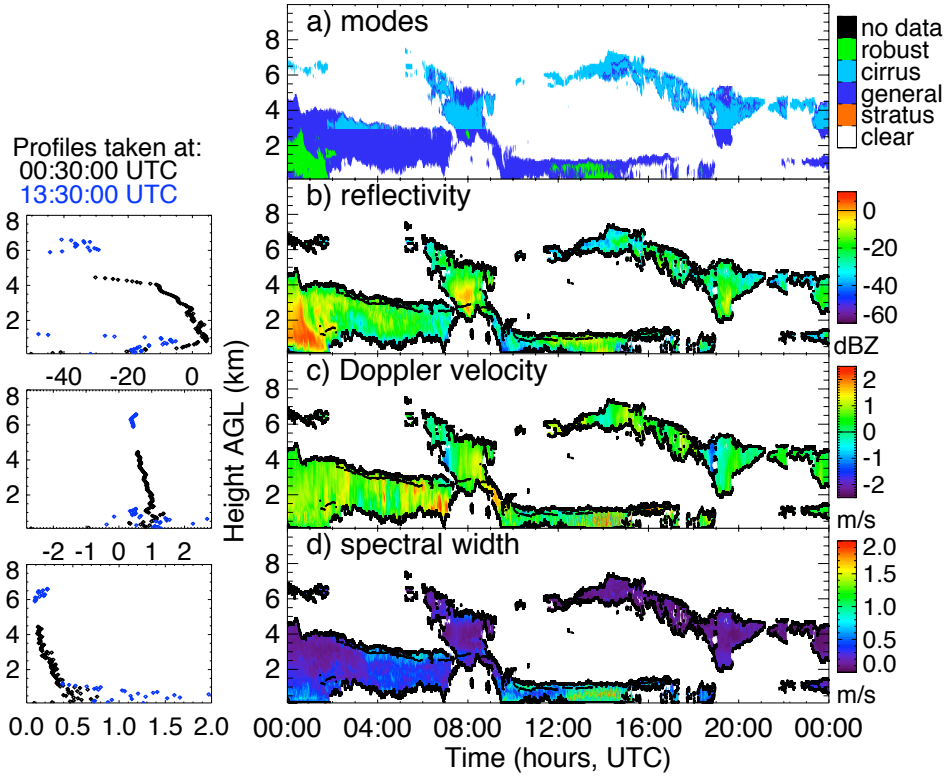

Figure 2–1: The MMCR modes (a) and measurements (reflectivity factor (b), Doppler velocity (c) and spectral width (d)) for September 9, 2005. The bold black lines are the radar echo boundaries, as defined in section 3.1, while the lighter black lines represent the cloud bases as seen by the AHSRL (see section 2.2.3). Profiles of the 10-s measurements taken at two different times are showed on the left.

low (below −20 dBZ), it is cloud particles. Further details on the exact threshold values, and their dependence on the phase of the sampled hydrometeors, are given in section 3.1. Nevertheless, the case of September 9, 2005 (illustrated in figure 2–1) provides a good example of that quick interpretation.

High values of reflectivity associated with downward velocities peaking at more than 1 m/s indicate that the first observed cloud on that day produced precipitation, which most likely reached the ground until 02 UTC (as the echoes started at the

lowest resolved altitude), while only virga[2] was falling afterward. From around 10 to 16 UTC, a stratus cloud passed, precipitating until 15 UTC. The first couple of hours, it might have been simply virga (some echoes are down to 95 m, but only with very low reflectivity values), while the falling particles were most probably liquid after 12 UTC (the velocities and spectral width are quite high, with some velocity folding happening). Between those two main systems (from 06 to 09 UTC), a higher cloud was observed, which might have produced virga that merged into the stratus layer. Around 12 UTC, another layer formed and it might have produced some virga between 19 and 20 UTC, as downward velocity and higher reflectivity values existed in conjunction with a sudden plunge of its base. The MMCR detected additional features on that day, but this information is not enough to say more about them.

2.2 Arctic High Spectral Resolution Lidar (AHSRL)

The first design of an HSRL was developed by a group of researchers at the University of Wisconsin-Madison, in order to study the optical properties of aerosols during day and night (Shipley et al., 1983). The main difference from a traditional lidar system is the use of a filter to isolate the part of the received signal caused by molecules (Rayleigh scattering), to then use it as a reference to compute the particulate signal (caused by Mie scattering), which will be absolutely calibrated without any *a priori* assumptions about the atmospheric attenuation. However, the

[2] *Virga* is a meteorological phenomenon characterized by the complete evaporation of the precipitating particles before they can reach the ground.

filter originally used was not precise enough to allow accurate sensing of dense liquid clouds, and a few related changes were required (Piironen and Eloranta, 1994).

Additional modifications were needed to fit the operating system to the requirements of Arctic observations, such as long-term unattended operations and low clouds dominance (Eloranta, 2005; Eloranta et al., 2004; Razenkov et al., 2002). This latest design makes up the AHSRL used at Eureka, which is controlled and operated remotely at the University of Wisconsin-Madison, by the lidar research group.

2.2.1 Technical Characteristics

The AHSRL works with a much smaller wavelength than the MMCR. In fact, its signal is in the visible, more precisely in the green, at 532 nm. With such a small wavelength, the lidar operates in the optic regime for all particulate matter (aerosols, hydrometeors...), since they usually have a diameter larger than a micron. Consequently, the returned signal is proportional to the number of particles and to the squared particle size ($N(D)D^2$). Thus, the AHSRL is more sensitive to the number of particles than to their size, which makes it a good complementary instrument to the MMCR.

Table 2–2 summarizes the main technical characteristics of the AHSRL, for both its transmitter and receiver parts. The very narrow receiver field of view protects the signal from most of the contaminations produced by multiple-scattering and, with the help of a skylight background filter, by solar background noise, ensuring a "clear" echo (Eloranta, 2005). However, to operate correctly with such a small field of view, a stable alignment between the transmitter and receiver optical axis is required at

Table 2–2: List of the technical characteristics of the SEARCH's AHSRL operating at the Eureka site (de Boer and Eloranta, 2007; Eloranta, 2005).

Wavelength	532 nm
Average transmitted power	600 mW
Pulse repetition rate	4 kHz
Beam polarization	circular
Telescope diameter	40 cm
Angular field of view	45 μrad
Solar noise bandwidth	8 GHz
Time resolution (max.)	0.5 s
(this project)	180 s
Range resolution (max.)	7.5 m
(this project)	30 m
Height coverage (max.)	$\sim$ 0.01 to 35 km
(this project)	$\sim$ 0.07 to 12 km
Maximal optical depth	$\sim$4

all times, which is achieved through the use of the same telescope and related optics for both the transmitted signal and its received echo (Eloranta, 2005).

The narrow field of view, in conjunction with a high pulse repetition rate, limits the strength of the signal coming from near the AHSRL, allowing the profiles to start at a lower range than usual (around 75 m), while still extending over tens of kilometers. Furthermore, the use of a high repetition rate helps make the transmitted beam eye-safe, through the transmission of many lidar pulses with low peak power, in combination with its spread over the large area of the telescope, reducing its energy density. Moreover, the beam energy distribution is flattened during the expansion process, allowing for a higher possible transmitted power.

The beam sent in the atmosphere by the AHSRL has a given circular polarization and the system uses three detectors to measure the strength of different parts of the

echoes: the full signal, the molecular part, and the depolarization ratio. An iodine cell is used to filter out the particulate part from the received atmospheric signal, taking advantage of the Doppler broadening effect, which depends on the range of velocity encountered (Eloranta, 2005): the motion of particulate matter is dictated by the winds and turbulence, which slightly broadens the signal, while molecules move according to a random thermal motion, which has a much wider distribution and broadens the signal a lot. Consequently, the echo consists of the superposition of those two differently affected signals, both centred on the laser frequency. Thus, using a narrow optical filter, centred on that same frequency, allows the removal of the particulate spike, which explains the laser wavelength choice since it corresponds to the line 1109 of the iodine absorption spectrum.

Finally, the roof of the AHSRL housing includes a window on top of the telescope (see figure 1–3), to allow its signal to get in the atmosphere and back in the system. A normal glass window is sufficient since the beam is in the visible light. However, since the lidar is operated in a vertically pointing manner, that window needs some specific attention: it should be heated to melt any frozen particle that falls on it, and slightly slanted to prevent water accumulation (de Boer and Eloranta, 2007).

2.2.2 Measurements

The AHSRL sends a signal at its wavelength and looks at the energy that is backscattered to its telescope (as for the MMCR), resulting mainly from scattering on atmospheric particles and molecules, as the effects of other sources are minimized by the lidar design. The detection of that returned signal is done through three

channels, each giving a different insight on the sampled volume. These are the combined, molecular and cross-polarized signals.

As the radar, the AHSRL can resolve the distance to the echoes, using the time difference between transmission and reception. A lidar profile starts around 10 m above the instrument and can extend up to 35 km, with a resolution of 7.5 m (see table 2–2). However, the first few ranges are contaminated by scattered laser light, and the measurements become reliable around 75 m, which is still quite low (Eloranta et al., 2004). For this project, profiles are also cut off near 12 km (see table 2–2) since tropospheric clouds should be confined below this level in the Arctic.

From the three measured signals, the AHSRL automatically computes three quantities and stores them for every resolved height. First, the combined signal (Rayleigh and Mie) provides the attenuated backscatter cross-section per unit volume (in units of $(\text{m Sr})^{-1}$), which is simply the data as they could be obtained by traditional lidar systems. Then, the removal of the molecular signal (Rayleigh) gives the particulate backscatter cross-section per unit volume (simply referred to as the *backscatter* later, also in $(\text{m Sr})^{-1}$), which is absolutely calibrated. Finally, the circular depolarization ratio[3] (simply called *depolarization* later) is obtained from the cross-polarized signal.

The AHSRL continuously repeats those measurements, starting a new profile every 0.5 s, providing an excellent time resolution. Although no merging is needed

[3] The circular depolarization ratio (CDR) is related to the linear depolarization ratio (LDR) through this simple equation: $CDR = \frac{2\ LDR}{1-LDR}$.

here (only one mode is used by the AHSRL), measurements are usually averaged over a larger volume, in both time and space dimensions, to reduce the noise (de Boer and Eloranta, 2007). In this project for instance, 360 profiles are combined in a single one, while four successive data are averaged together along the vertical, resulting in final resolutions of 3 minutes and 30 m, respectively (see table 2–2).

An example of the lidar's data at those resolutions is given in figure 2–2 for measurements acquired on September 9, 2005 (the same day as in figure 2–1), along with two profiles (also corresponding to the ones in figure 2–1). Note the four data gaps around 00, 06, 12 and 18 UTC, caused by lidar systems calibrations. Even though they are done on a regular basis, their length varies from one another. Additional white areas in these images are due to an insufficient signal: the relative contribution of the particulate matter can only be retrieved when enough signal is returned to the lidar. This decrease in the maximum range accurately resolved by the AHSRL is the only effect of the attenuation on the retrievals, although it also creates some speckled results in areas where a small portion of the beam still went through. Furthermore, notice all the detailed structures revealed in panel (b) that were not visible in panel (a).

2.2.3 Interpretation

As for the MMCR, a quick look at the lidar measurements can give some information about the particles present in the observed region. For instance, the number density of the sampled particles can be derived from the backscatter value, since the lidar signal is dominated by the particles number concentration. Thus, if the backscatter is high, there are a lot of particles in that area, while if it is low, the

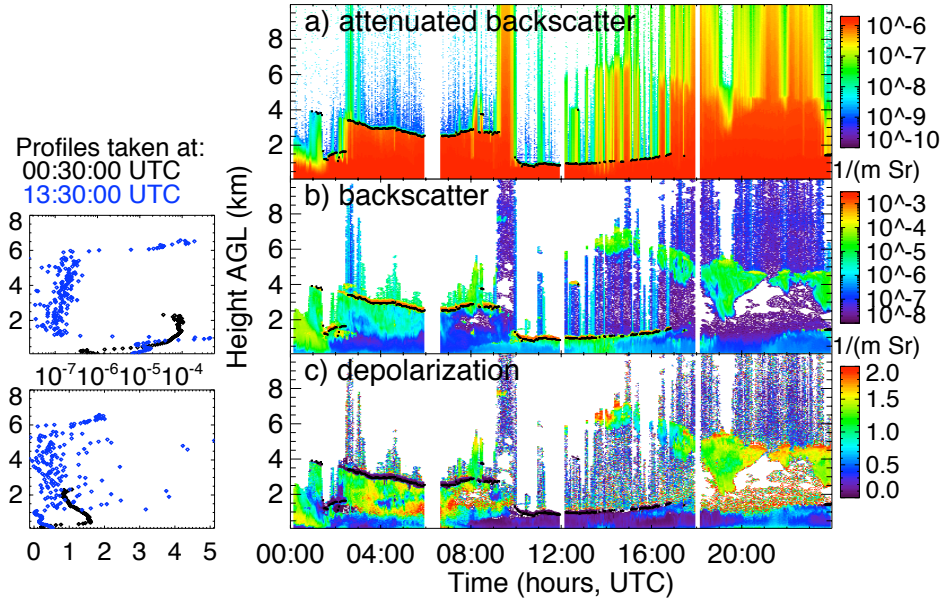

Figure 2–2: The AHSRL measurements (combined (a) and particulate (b) backscatter cross section per unit volume and (c) circular depolarization ratio) taken on September 9, 2005. The black lines represent the liquid cloud bases detected by the lidar. Profiles of the 3-min averaged measurements taken at two different times are showed on the left.

particles are less numerous and, if it is below a given threshold value, the area can be declared *clear*. On the other hand, the depolarization value indicates the degree of sphericity of the sampled particles. Since the more numerous particles dominate the signal, the derived result applies mostly to those. Consequently, if the depolarization is high, the more numerous particles are non-spherical, most probably implying ice crystals. At the opposite, if the depolarization is low, the majority of the particles are spherical, implying most certainly the presence of liquid particles.

Although the actual threshold values will be given in section 3.2, this quick interpretation can be applied to the case of September 9, 2005 (shown in figure 2–2). For instance, the vertically-narrow high-backscatter (red) regions are associated with

low-depolarization (dark) regions, marking the presence of many spherical particles, which are most probably cloud droplets. This is usually a good indicator of the cloud base position, shown as the thin black lines in both figures 2–1 and 2–2.

However, not all systems present that signature. This can be simply due to an absence of cloud droplets, as after 18 UTC: the AHSRL resolved the whole cloud (comparing with figure 2–1), finding high depolarization everywhere. Another explanation is the presence of strong attenuating particles in the lower levels, preventing the beam from reaching the cloud base, as during the first hour: no lidar signal is observed above 2.5 km while the radar image (see figure 2–1) indicates a cloud top 2 km higher than that. Moreover, high backscatter values are spreading over almost 2 km above the surface, most probably caused by numerous snowflakes, as the depolarization is also quite high.

Usually, most of the high-backscatter regions (light blue and above) in figure 2–2 are associated with relatively high depolarization values (green and above), indicating that the hydrometeors were dominantly in a solid phase on that day. The only exceptions are found in the cloud base signatures (already discussed) and in the lowest kilometre from around 08 to 19 UTC. This implies liquid precipitation, as it is below a cloud base but does not depolarize the signal. Finally, the low-backscatter (purple) regions are most likely indicating clear atmosphere.

Although the AHSRL can accurately show which areas contained liquid, it cannot easily tell if solid hydrometeors were also present, as the signal is dominated by the more numerous particles and some crystals tend to align themselves in such a way that the depolarization signature is similar to the liquid phase. Consequently, lidar

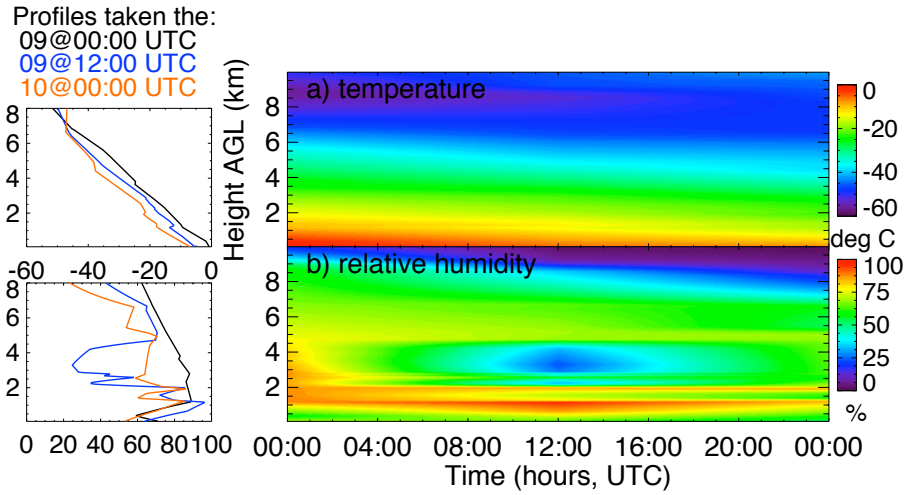

Figure 2–3: The temperature (a) and relative humidity (b) fields obtained from the rawinsondes profiles retrieved at Eureka on September 9, 2005 (shown on the left).

data alone are not sufficient enough for this project, and they have to be combined with others (mostly the radar data here).

2.3 Benefits of Instrument Synergy

As shown in the middle panel of figure 1–3, the Eureka MMCR and AHSRL have been installed side by side in the same seatainer. That way, it is easy to compare and combine the measurements of both instruments together: they are basically looking at the same part of the atmosphere. Moreover, rawinsondes are launched directly at Eureka's weather station, less than 1 km to the South of the ØPAL facility, normally at 00 and 12 UTC, as part of the World Meteorological Organization (WMO) radiosondes network. The left panels of figure 2–3 shows the retrieved temperature profiles for September 9, 2005 (the same day as in figures 2–1 and 2–2), as well as the profiles of relative humidity, computed from the temperature, pressure and dew point profiles.

The combination of the various data sets must account for the different resolutions. Here, when measurements from more than one instrument are combined, the lidar time-height grid is used. Thus, the radar data are vertically interpolated, while averaged in time, and the recovered sounding data, which are already provided with the same vertical resolution as the lidar data, are simply interpolated in time (see the right panels of figure 2–3). This can lead to major uncertainties as soundings are taken hours apart, especially for the fast-varying variables like the relative humidity (see figure 2–3b). Therefore, only the temperature field will be used here.

This synergy allows a better characterization of the clouds passing over Eureka. For instance, the lidar usually gives a more accurate estimation of the cloud base height for the liquid and mixed-phase clouds. However, its signal gets quickly attenuated by the liquid cloud droplets, preventing it from seeing the cloud top that is usually well observed by the radar (as around 08 UTC on September 9, 2005). Furthermore, the attenuation from a cloud layer is sometimes such that the lidar cannot resolve the higher layers as well (see near 16 UTC on September 9, 2005). Nevertheless, the AHSRL is more sensitive than the MMCR, resulting in lidar detections of thinner clouds (not used here) and aerosol layers (not fully exploited, as clouds are the main interest here).

Finally, the simultaneous use of all the measurements facilitates greatly the phase characterization of the cloud and precipitation particles. For instance, the temperature fields define some crucial points (such as the -40 and 0°C levels), while the lidar depolarization distinguishes the spherical particles.

Chapter 3
Methodology

In atmospheric science, as in many other disciplines, the quality of the measurements critically depends on the suitability and sensitivity of the sensors used. Additional critical factors are the assumptions involved in the inversion of the instruments observables (such as radar reflectivity and lidar depolarization) to cloud and precipitation variables (cloud fraction, boundaries, phase...). Thus, it is imperative to develop an objective methodology in order to study cloud and precipitation properties using a radar/lidar synergy. Here, examples of measurements from the MMCR and AHSRL (taken on September 9, 2005, as in chapter 2) are used to demonstrate the advantages and disadvantages of each instruments and the power of their synergy, as well as to present the assumptions involved in the data interpretation.

With two years of data taken every three minutes, or even 10 seconds, some averaging of the results is necessary before performing the analysis on their time series, in order to be able to distinguish some features. Consequently, most of them will be represented by the fraction of time that the characteristic was observed over a given period, which length depends mostly on the extent of the studied time period: hourly averages should be used for the observations done in less than a week (as in this chapter), while daily to monthly averages are better suited for data spreading over longer periods. When applicable, some results will be shown as a single value (the mean) with errorbars (one standard deviation from that mean).

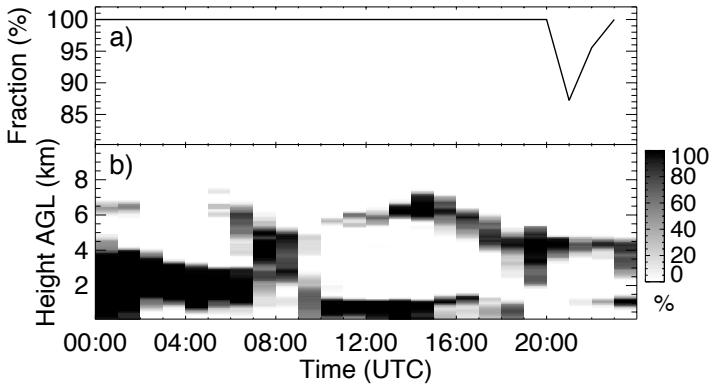

Figure 3–1: Vertically integrated (a) and resolved (b) hourly occurrences of hydrometeors (cloud and precipitation particles) for September 09, 2005.

3.1 Hydrometeor Occurrence and Layers

A simple (but subjective, as it depends on the instrument used) definition of a cloud occurrence makes use of the MMCR high sensitivity: cloud is detected whenever its reflectivity factor is greater than -60 dBZ, which represents the minimum detectable signal of the MMCR from the surface to the tropopause. Obviously, that criterion includes also the precipitation size particles, and maybe even some aerosols. The fractional coverage of all those detected hydrometeors can then be computed as the fraction of time that criterion was met at a given height, the *vertically resolved* hydrometeor fraction, or at any height, the *vertically integrated* hydrometeor fraction (see figure 3–1 for an example of the results). The almost continuous cloud cover seen in figure 3–1a was also observed at Eureka's weather station, which was reporting at least "mostly cloudy" conditions at every hour (see the EC archives).

Hydrometeors tend to occupy an area (a *layer* as referred to later) of the atmosphere observed by the vertically pointing instruments. These different hydrometeor layers interact through scattering, absorption and emission with radiation and, thus,

drastically affect the radiation budget of the Earth's surface, atmosphere and top. Therefore, it is important to record the number of hydrometeor layers and their corresponding boundaries (base, top and thickness). In a given vertical atmospheric profile, a layer is defined as a group of pixels classified as hydrometeors, with the base and top respectively taken as the lowest and highest heights satisfying the −60 dBZ criterion (for an example, see figure 2–1 where the thick black lines actually represent those layer boundaries for the illustrated case). The number of hydrometeor layers is then simply the number of such hydrometeors groups detected within the profile and its variation with time is rather easy to follow.

All detected hydrometeor layers contain cloud particles and, sometimes, also precipitation ones. However, exceptions might arise. For example, a cloud can end its life by transforming all its particles to precipitation, which represents only a small fraction of the layer's life. Moreover, blowing snow and fog occurrence could be confused with precipitation without a corresponding cloud, but those phenomena rarely get high enough (the radar "dead zone" is 95 m) to be detected by the radar. Finally, the sensitivity of the MMCR is greater at closest range, which could allow it to detect low-level aerosols, without any cloud associated with them. However, these non-hydrometeor layers are rarely seen by the MMCR, as most aerosols are still too small to be detected. Overall, those phenomena have a negligible effect on the final results, even when considered all together, as they represent only a small fraction of the studied time, spread over longer periods than the averaging time.

This simple layer definition allows us to track with time the number of hydrometeor layers observed in the troposphere and their associated boundaries. This

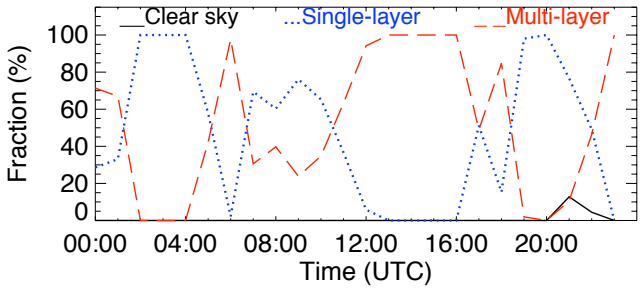

Figure 3–2: Hourly occurrences of the different cloud systems for September 09, 2005. The solid black line represents the clear sky condition, while the dotted blue and dashed red lines show respectively the single- and multi-layer systems.

is important, since the cloud radiative forcing strongly depends on the number of layers and their vertical distribution, that dictates their phase. Thus, three cloud systems are defined based mainly on the number of layers: i) *clear sky* when no radar echo was detected, ii) *single-layer* when only one hydrometeor layer was found, and iii) *multi-layer* when two or more hydrometeor layers were observed. Recording which system was observed in every radar profile allows an averaged occurrence for each system to be computed over a given time period, as in figure 3–2.

3.2 Phase Classification

As briefly discussed in section 2.2.2, the hydrometeor phase can be derived from the AHSRL measurements, since the backscatter intensity and depolarization ratio are good indicators of, respectively, the number concentration and shape of the small and more numerous particles (de Boer and Eloranta, 2007; Shupe, 2007). For example, aerosol particles, although found in large concentrations compare to liquid and ice particles, produce very low backscatter values because of their small sizes ranging from nanometers to microns. Furthermore, below a certain lidar backscatter value (see figure 3–3), the area is considered clear from Mie scatterers (such as

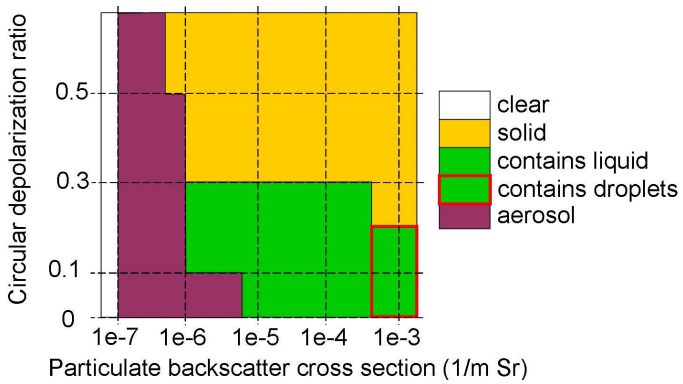

Figure 3–3: AHSRL classification based on the combination of its backscatter and depolarization measurements. The red box indicates the criteria to find cloud droplets.

hydrometeors, dust and aerosols). Those pixels cannot cause strong radar echoes. Thus, that classification is kept only if the associated MMCR reflectivity is lower than -50 dBZ. Otherwise, we assume that hydrometeors were present, but their phase is classified as *unknown*.

On the contrary, high lidar backscatter indicates the presence of hydrometeors and lidar depolarization measurements are required in order to distinguish spherical (liquid) from non-spherical (ice) particles. The AHSRL detects near zero depolarization from liquid drops, since the beam reflects mostly on their front and rear surfaces, which preserves the polarization (Sassen, 2005). Moreover, hydrometeor concentration decreases with size. Consequently, the regions characterized by high values of backscatter associated with low values of depolarization are assumed to contain cloud droplets (see figure 3–3 for all the thresholds values).

On the other hand, ice crystals and snowflakes are non-spherical, depolarizing the lidar signal more through the internal reflections and refractions of the laser beam (Sassen, 2005). In some instances, crystal plates tend to align themselves horizontally

in particular situations (as in some cirrus clouds), such that the depolarization stays in low values for vertically pointing lidars (Sassen, 2005). When both phases (liquid and solid) coexist in a sampled volume, the depolarization profile is dominated by the near-zero values of the liquid droplets that are typically found in concentrations orders of magnitude higher than ice particles. In this case, the presence of non-spherical particles cannot be excluded.

Temperature measurements from soundings, interpolated in a grid that matches the lidar data resolutions, can refine this phase classification. Solid particles are unlikely to exist above 0℃, and any hydrometeor found in such warm areas is classified as liquid. Moreover, it is believed that any liquid water particle whose temperature drops below −40℃ will freeze homogeneously, almost instantaneously (as observed by Shupe et al. (2006) and many others), and hydrometeors found in such cold areas are all classified as solid. Between those limits, both phases can exist and the previous classification is kept. Radar measurements can provide some final refinements. If the particles appear to be falling faster than 2.5 m/s, they are most likely liquid drops, as it is highly unlikely to have solid particles with a Doppler speed that high in the Arctic. Furthermore, any region characterized by an MMCR reflectivity above −60 dBZ that has not been classified yet is put in the unknown class.

Once the precipitating regions are known (see section 3.3), the pixels classified as mixed-phase are re-classified. Liquid droplets can coexist with ice particles in cloud areas, but not in precipitation (based on Shupe, 2007): the air can contain less water vapor in presence of ice than in presence of liquid, favouring the growth of ice crystals at the expense of the droplets in mixed-phase clouds, and the solid particles

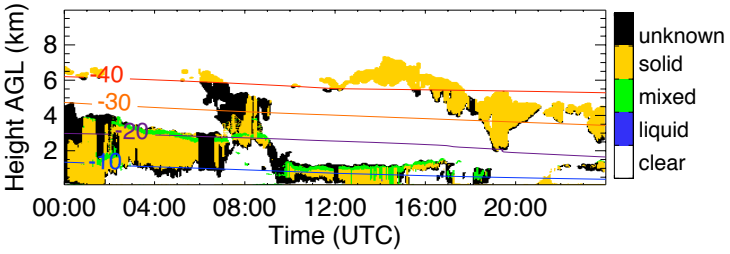

Figure 3–4: Result of the phase classification for September 09, 2005. The lines represent the isotherms given at intervals of 10°C.

will fall on their own. Therefore, any precipitating regions that have been classified as mixed-phase must be reviewed: they are either only liquid drops (if the Doppler velocity is greater than 2.5 m/s) or only ice crystals (otherwise).

An example of the result is given in figure 3–4, which shows different structures of hydrometeor phase. For instance, the echoes around 6 km and higher are entirely made of ice particles, based on the temperature criteria (as shown by the −40°C isotherm). Also, some liquid are found, mixed with ice particles, as high as 4 km, corresponding to a temperature of approximately −25°C. However, those seem to be confined in thin layers near the top of the radar echo layers (most probably also near the cloud base), as ice particles are mostly found alone below those layers, as expected. Although a mixed-phase layer usually represents only a small fraction of the volumes of hydrometeors found in a profile, it was present throughout most of the day, as emphasized in figure 3–5d with the time series of the hourly occurrences of liquid (alone or mixed with some crystals).

The unknown phase classification is often found at the lidar calibration times, each six hours apart, with a varying duration. However, there are two other causes

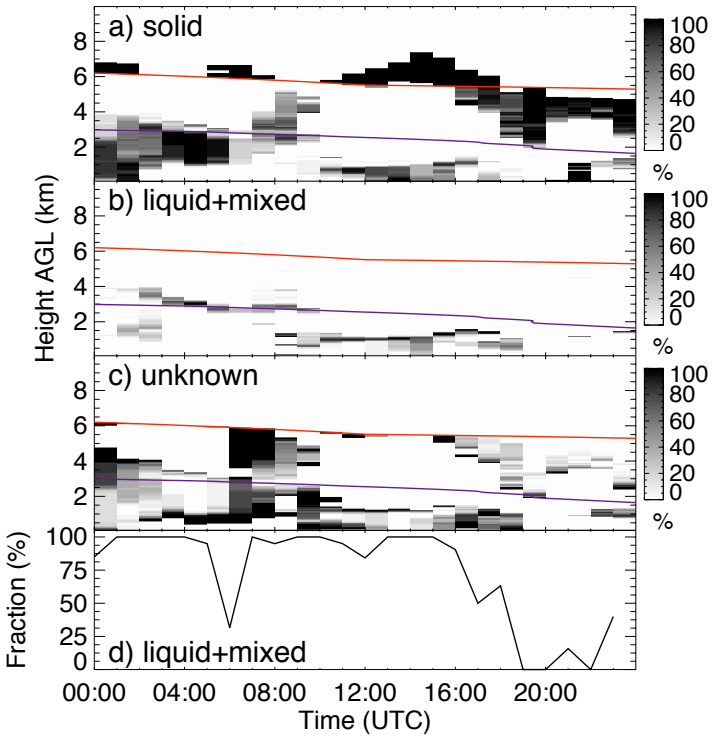

Figure 3–5: Vertical distribution of the hourly occurrences of the (a) solid, (b) liquid and (c) unknown hydrometeor phases and (d) hourly integrated occurrences of liquid for September 09, 2005. The liquid phase include the mixed-phase occurrences. The lines in (a-c) represent the −20 and −40°C isotherms.

that render the phase classification impossible. First, the lidar data become unreliable after the beam went through a layer of dense and/or absorbing particles, such as a liquid cloud base (as around the middle of the day in figure 3–4) or heavy precipitation (as during the first hour). This happens more often during the summer months, when liquid is likely to occur in greater amounts, such that the lidar signal gets too attenuated for any retrievals to be trusted. The second case is when radar echoes are classified as aerosols by the lidar, and it was necessary to bring them back to hydrometeors without a known phase, especially near the base of layers that seem

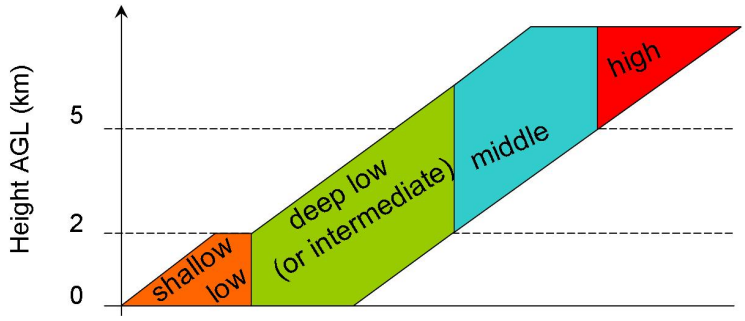

Figure 3–6: Criteria for the cloud types classification, based on their base and top heights, with the combination of the shallow and deep low providing the low class.

to have produced virga (as between 04 and 05 UTC in figure 3–4). All those observations are still visible after averaging, for each hour and at every resolved height, the fraction of hydrometeors that were in a given category, as depicted in figure 3–5a-c.

3.3 Cloud Identification

Based on their morphology (mostly their base and thickness), the cloud layers observed can be classified into three types: i) *high* (or cirrus) clouds with bases higher than 5 km, ii) *middle* (or alto) clouds have their base between 2 and 5 km, and iii) *low* (including both stratus and cumulus) clouds have their base below 2 km. The latter category can be further divided into the *shallow* (or boundary layer) and *deep* (or intermediate) systems, that are respectively confined below and extending above the 2-km level (see figure 3–6 for a complete reference). Those definitions closely relate to the usual tropospheric levels in the Arctic: as in any other region, the boundary layer extends from the surface up to an altitude of 2 km, while the high troposphere starts at 5 km, since the tropopause arises lower (around 10 to 12 km), and the middle troposphere is found between those limit altitudes.

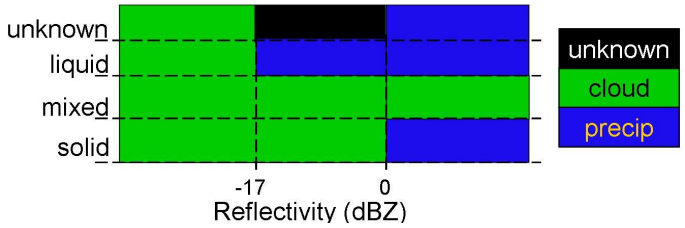

Figure 3–7: MMCR reflectivity threshold values used for the differentiation of the echo between cloud and precipitation, for the different hydrometeor phase.

Unlike the layer systems, the cloud types are obviously highly dependent on the definition of cloud occurrence. Consequently, the success of their separation from the precipitation and aerosol echoes is of crucial importance. A preliminary separation can be made using simply the MMCR reflectivity factor, as shown in figure 3–7, with threshold values varying with the phase of the hydrometeors (as found in section 3.2). For liquid particles, the separation is well defined (Frisch et al., 1995): only cloud droplets are present if that quantity is lower than -17 dBZ, while some precipitation-size particles must be present to explain higher values of radar reflectivity.

On the other hand, no consensus exists on a similar, well-defined, threshold value for the solid particles. In fact, the exact value probably depends upon many factors, such as the crystals shape(s) (Hong, 2007). Consequently, values ranging from -15 to 5 dBZ can be found in the literature (Shupe, 2007; Shupe et al., 2005). For this project, a conservative threshold was chosen (0 dBZ) to avoid most of the misclassification of echoes as precipitating ice.

On the contrary, no threshold was used for the mixed-phase pixels (all are considered clouds). This comes from the fact that ice crystals grow faster and at the expense of the liquid droplets. Thus, the precipitation should all be solid below a

mixed-phase cloud, with mixed-phase precipitation rarely occurring. Consequently, all mixed-phase echoes are classified as clouds. However, if the phase is unknown, the two previous threshold values are used: cloud and precipitating particles are assumed for reflectivity factors respectively below −17 dBZ and above 0 dBZ, while the type remains unknown otherwise.

The lidar provides the means for a more robust classification. First, clouds that contain liquid will usually be recognized by the presence of cloud droplets throughout their depth: when the ascending air saturates at the cloud base, water vapor starts condensing into droplets, which will grow while they follow the updraft up to the cloud top (Rogers and Yau, 1989). As a consequence, cloud liquid is in highest concentration at the base, where the droplets first form and are the smallest. Thus, the cloud base is defined as the first lidar detection of a high concentration of spherical particles (see the red box in figure 3–3). Inside a radar echo layer containing such a signal, all valid radar echoes above it are set to cloud, while those below are said to be caused by precipitation. This works mostly for the first layer of clouds containing liquid, as the lidar beam gets attenuated by the numerous droplets.

Moreover, some lidar backscatter values (see figure 3–3) indicate the presence of aerosols instead of hydrometeors, which are not made of water (hence, have no phase classification) and are not studied here. However, this classification is only kept if the associated radar reflectivity is lower than −50 dBZ. Finally, any pixel with a Doppler velocity greater than 2.5 m/s downwards is most certainly caused by falling particles, as downdrafts of that strength are unlikely in the Arctic (Shupe, 2007; Shupe et al., 2008a).

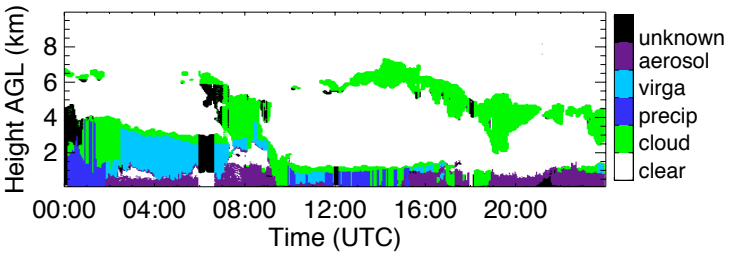

Figure 3–8: Result of the echo classification for September 09, 2005.

Between and above radar layers, the atmosphere is declared *clear* as the lidar measurements are less reliable due to the lower layers attenuation. However, since this algorithm uses measurements from both the MMCR and AHSRL, if either of them is not available throughout the column, the algorithm is not applied and the pixels are set to an *unknown* type. The only exception arises when the temperature is below −40℃ or above 0℃, in which cases the phase is known with certitude and the algorithm can then be applied. An example of the result is given in figure 3–8, where the echoes classified as precipitating have been further divided into virga and actual precipitation, with the radar echoes of the latter extending below 200 m.

In the profiles containing virga, aerosols are usually observed beneath it, indicating that the hydrometeors evaporated or sublimated (depending on their phase), leaving only their nuclei. Furthermore, aerosols were continuously present in the boundary layer, especially up to around one kilometer high. As for the actual distinction between cloud and falling particles, it seems to be rather robust. There are some echoes reaching low heights that were classified as cloud, but this happens mostly when the precipitation shaft forms (around 10 UTC) or dissipates (after 14 UTC). Moreover, Eureka's weather station reported "snow" conditions twice that day (EC

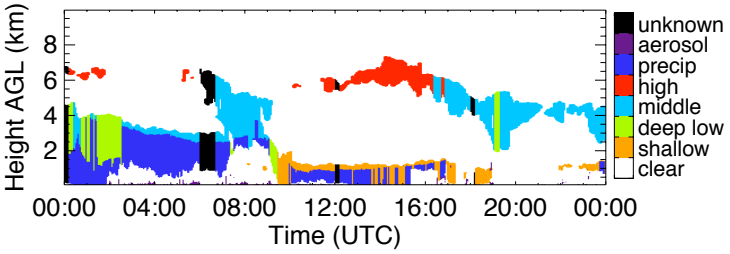

Figure 3–9: Cloud types observed on September 09, 2005.

archives), corresponding to the precipitating hours seen here (01 and 13 UTC), which were detected as solid particles (see figure 3–4). Finally, the higher layers that are entirely made of ice never precipitated according to that classification, although it often looks like virga was being produced, especially between 19 and 20 UTC: the radar echo base quickly dropped from 3.5 to 2 km, creating a parallelogram-shaped echo return in the lowest kilometre of that part of the layer. This emphasizes the difficulty of differentiating cloud ice from falling snow. Overall, the result looks plausible, despite the complexity of the case.

In figure 3–8, the new cloud boundaries are clearly visible, especially in profiles where all echoes are actually classified. For further analysis of the clouds, the unknown category was considered as cloud, unless that classification came from missing data of either instrument throughout the column. Using those newly-defined boundaries, the type of each observed cloud layer can be derived in every profile, as shown in figure 3–9. Then, the averaged occurrence of each cloud type can be followed throughout the period, as well as their precipitating fractions (see figure 3–10). Furthermore, an investigation of the combinations of cloud types is possible.

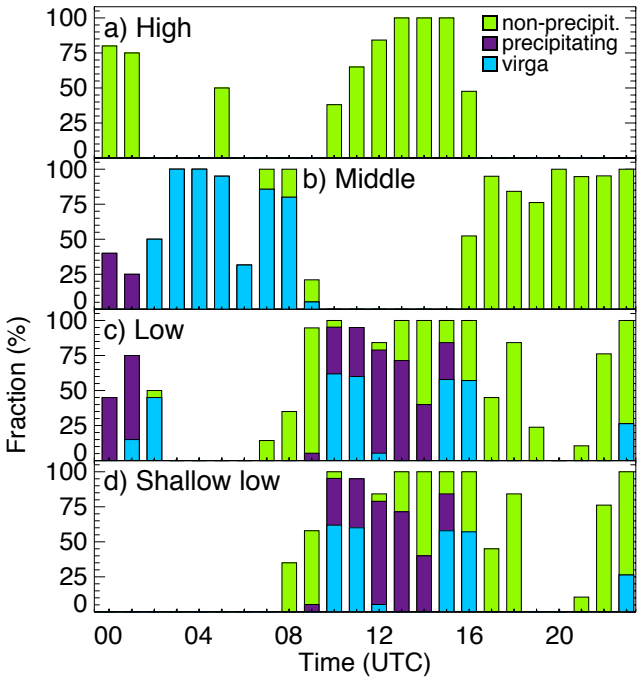

Figure 3–10: Hourly fraction of (a) high, (b) middle, (c) low and (d) shallow low clouds observed on September 09, 2005. The lower part of each bar indicates the fraction of the hour that type was precipitating, as ground precipitation (dark blue) or virga (light blue) the ground.

Chapter 4
Results and Discussion

The most important requirement for the development of a climatology is the collection of a continuous and high quality record of observations. The operational status of the instruments used in this study is shown in figure 4–1. Each group of columns represents the fraction of time in each month that the instruments were working properly for more than 50% of a day, alone and together. Figure 4–1 emphasizes the reliability of the active sensors to operate on a unattended manner for a prolonged time period, which is an achievement in itself, especially when considering the remote nature of the location. In mid-July 2006, the lidar experienced hardware failure (the laser output power dropped very low), causing a downtime that lasted almost the entire month of August 2006. A similar failure in the AHSRL occurred in April 2007, but it was resolved more quickly, with the lidar back on working mode in May 2007. Nevertheless, both of these major downtimes took place during or near the summer, when other means exist to characterize the cloudiness of the sky.

No major downtime occurred for the MMCR during the studied period, and it continuously profiled the troposphere more than 75% of every month. Thus, the results obtained from the MMCR data alone (the cloudiness and clouds overlap) are continuous and can be used to illuminate the cloud and precipitation climatology of the studied period. However, the cloud and precipitation properties retrieved from synergetic measurements of the lidar and the radar (hydrometeor phase and

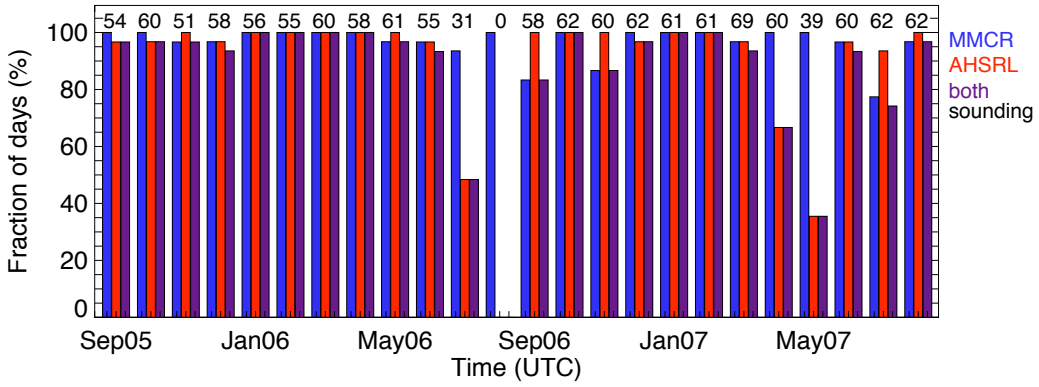

Figure 4–1: Fraction of days within each month of the two-year period that the MMCR and the AHSRL were properly working, alone (respectively blue and red) and together (purple), more than 50% of the time. The numbers above each group of columns represent the number of sounding profiles provided within each month.

cloud types) are available only during days that both instruments were operational, creating small gaps in their climatology over the studied period.

For every month considered here, the total number of retrieved temperature and humidity profiles from the atmospheric soundings is also indicated in figure 4–1. Like other locations in the world, rawinsondes are launched at Eureka on a regular basis, at 00 and 12 UTC of each day. However, malfunctions of the recording ground-based receiver or the thermodynamic sensors and/or bad weather that makes the balloon launch difficult can disrupt the record of atmospheric soundings. On occasions, balloons are also launched between those scheduled times, to either compensate such a gap or simply satisfy a scientific interest. As a consequence, the number of rawinsondes is larger than two times the number of days for some months, such as March 2007. The soundings used in this study were available through the lidar files. Thus, soundings are missing when no corresponding lidar data were reported. Despite these issues, profiles were usually available twice daily when it matters most:

when the phase classification is done (i.e. when both the MMCR and AHSRL were properly working).

4.1 Climatology

A first interesting result is the occurrence of hydrometeors. As shown in figure 4–2a, they dominated the two-year weather with monthly occurrences over 60% for almost every month, except during the spring transition, when clear skies are often encountered and the fraction of hydrometeors dropped below 50%. Despite the high monthly-averaged hydrometeor fractions, a small seasonal variability of the monthly-averaged coverage is visible. A small trend of decreasing monthly-averaged hydrometeor fraction is perceived during the winter months, with a minimum observed during the transition between spring and summer. Then, the monthly-averaged hydrometeor fraction increases quickly to its maximum throughout the summer and fall. Although more observations are needed to verify the existence of that cycle (those two years show a great variability in the timing of the regime changes), previous studies done elsewhere in the Arctic showed the presence of a similar cycle (Curry et al., 1996; Intrieri et al., 2002; Walsh et al., 2008).

The minimum occurrence is likely linked to the return of the sun (in the second half of February, with the polar day starting in mid-April), as in the marine stratocumulus clouds diurnal cycle (Duynkerke and Teixeira, 2001), although other factors are needed here to explain the varying timing. Such factors might be the opening of the water around the Eureka area. However, the fjord opens too late (toward the end of July every year), eliminating that hypothesis. The origin of the airmass might also influence the thermodynamic state of the atmosphere and, as a result, the

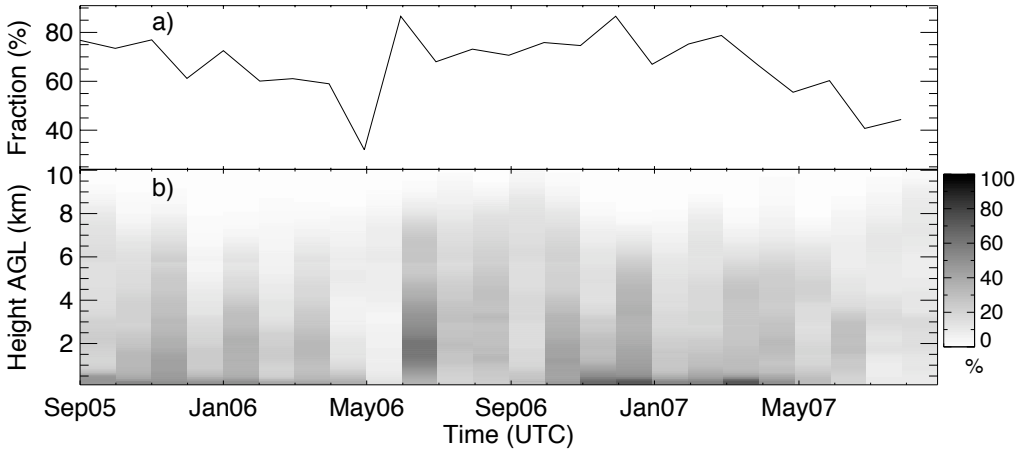

Figure 4–2: Time series of the monthly averaged occurrence of hydrometeors (a) and its dependence on height (b) for the two years.

hydrometeor fraction in the tropospheric column. That cause can be investigated from the horizontal wind distribution. Figure 4–3 compares their direction and speed within winter and summer[1] seasons for different levels of the troposphere, as measured by Eureka's rawinsondes. During the winter months, the low-level winds are dominantly coming from the SSE[2] to South, NE and NNW, which also tend to have the highest wind speeds. During the summer, those preferences are also observed although the NNW peak is spreading toward the West, where the stongest winds are coming from. Those features are influenced by the strong topography and water

[1] The usual definition of seasons were used throughout this work: winter includes the months of December through February, while the months of June through August represent summer.

[2] Throughout the following discussion, the wind directions are abbreviated using combinations of the usual letters for the four cardinal points (N for North, E for East, S for South and W for West) to represent the typical intermediate directions.

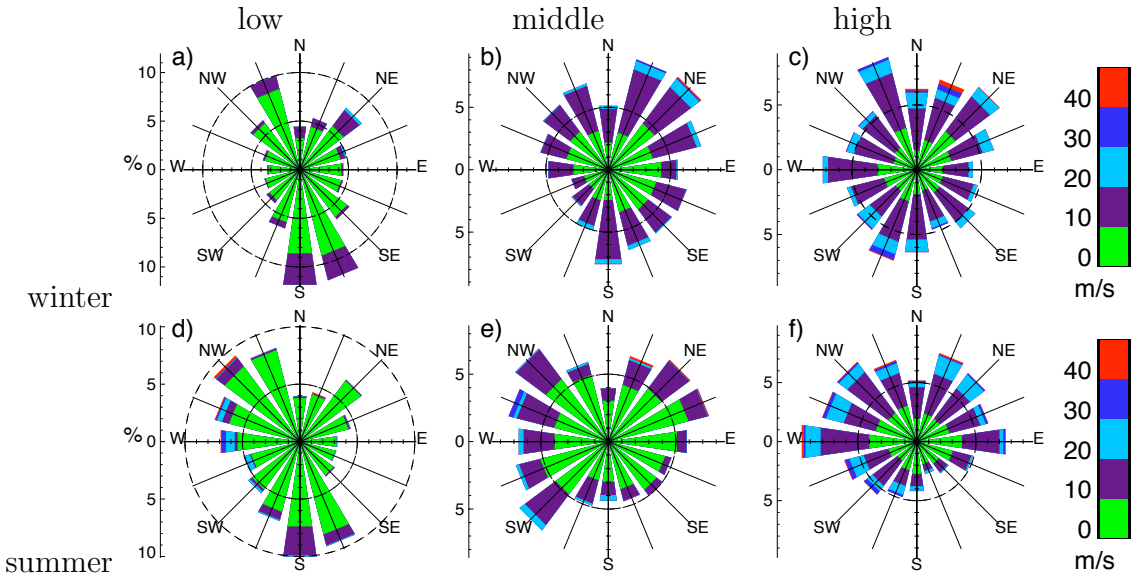

Figure 4–3: Distribution of the wind direction and speed during the winter (a–c) and summer (d–f) months for all situations, as found within the first 2 km of the troposphere (left), between 2 and 5 km (center) and above 5 km (right).

channels surrounding Eureka (see figure 1–2), which play a critical role in dictating the low-level wind direction in all seasons. In the middle troposphere, the summer distribution peaks from SW to NW and bottoms around the South, while the contrary happens during the winter. In the upper troposphere, the summer distribution indicates a West-East alignment and a lack of southern winds.

These observations seem to indicate that a fjord channelling might be associated with cloud formation, since both are mostly found during the summer. Additional analysis of the winds was conducted, partitioning the wind speed and direction between clear and cloudy conditions (figure 4–4). The main difference is the fact that those situations are characterized by opposite wind directions: at all levels, the clear cases are characterized by a strong preference for the NE or ENE winds (where a

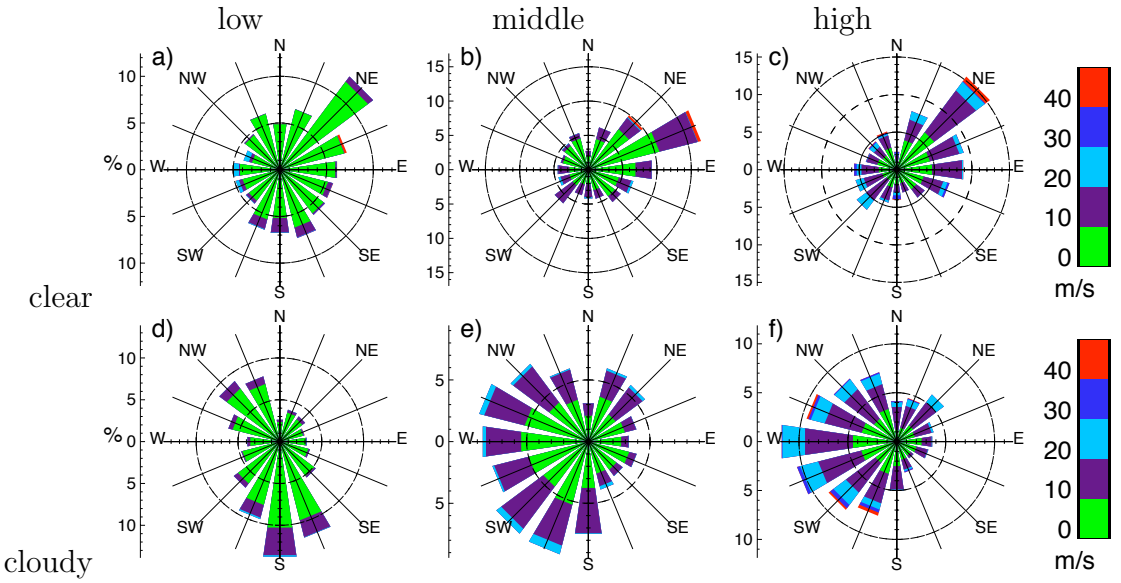

Figure 4–4: Distribution of the wind direction and speed during clear (a–c) and cloudy (d–f) cases, as found within the first 2 km of the troposphere (left), between 2 and 5 km (center) and above 5 km (right).

high valley is found between big mountains), as opposed to clouds occurring under winds from anywhere between NNW and SSW (along water channels valleys) above 2 km and a strong channelling below along the water bodies. The high-level wind patterns might be linked to the synoptic-scale patterns that dictate subsidence and ascent on large scale (causing cloudy and clear conditions), which might also cause a different low-level channelling by guiding the wind through the various mountains.

A different way to look at the hydrometeors occurrence is to include the height dependence of their coverage within each month, as depicted in figure 4–2b. This shows that hydrometeors are more often observed in the lower troposphere during the colder months (the polar night and a little after, especially for the second year) than during the warmer months (the summer season). Figure 4–5 illuminates the

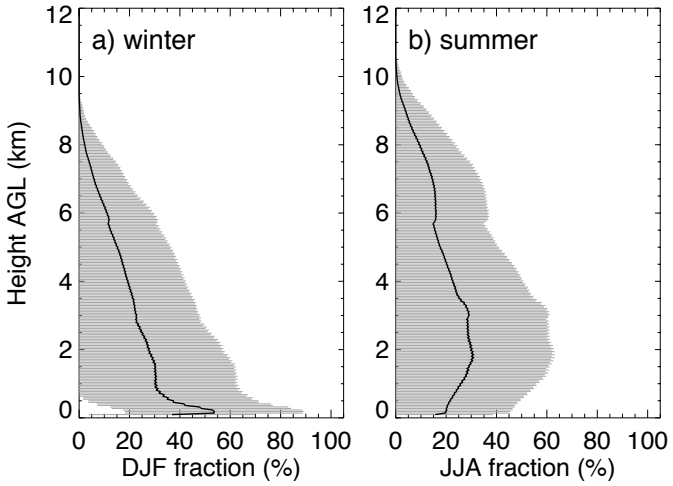

Figure 4–5: Distribution of the daily hydrometeor fraction with height for the two (a) winter and (b) summer seasons. The thick curves represent the mean of the fractions, while the horizontal grey lines are the standard deviations from that mean obtained at each range gate.

contrast between winter and summer months, where it is greater, indicating that the boundary layer tends to be cloudy (or precipitating) during most of the winter. Contributing factors for the low-level cloudiness observed during the winter is the lack of sunlight and the development of a temperature inversion that limits the vertical development of the clouds. In these shallow cloud layers, vertical mixing is often maintained through cloud-top radiative cooling, thus increasing their persistence. On the contrary, during the summer, the sun is always shining. Thus, these processes disappear, allowing clouds to form higher and develop more vertically. An equal spread of the coverage is then observed, although there seems to be a slight maximum in the lower part of the middle troposphere, between 2 and 3 km.

It can also be observed in figures 4–2b and 4–5 that the maximum height of the clouds is dictated by the tropopause altitude, as expected, which is lower when the

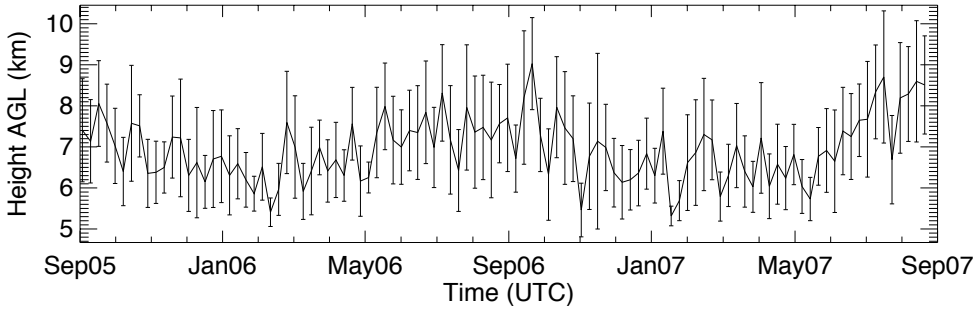

Figure 4–6: Time series of the mean highest cirrus top height (and its standard deviation) observed on a weekly basis over the two years.

troposphere is colder (during winter). A time series of the highest cirrus top height, such as in figure 4–6, demonstrates that feature better. Only the cirrus clouds are considered here, since they are the ones affected by the tropopause height. An annual cycle is clearly depicted in figure 4–6, showing lower heights during the wintertime. The tropopause height is the most likely limiting factor that caused that cycle. Other variations are visible (weekly and even shorter ones from the standard deviation around the mean) and can also have been caused by the tropopause variability, as well as other factors such as the synoptic condition and airmass origin, although related to the former.

Another interesting feature is the relationship of different cloud types and their ability to create precipitation. A nice way to study those characteristics is to look at the time series of the occurrence of various cloud types (see section 3.3 for their description), as well as their precipitating time fraction, as in figure 4–7. It is important to remember that the gaps around July 2006 and May 2007 are caused by the major lidar's downtimes instead of real clear times, and the surrounding results might be affected as well.

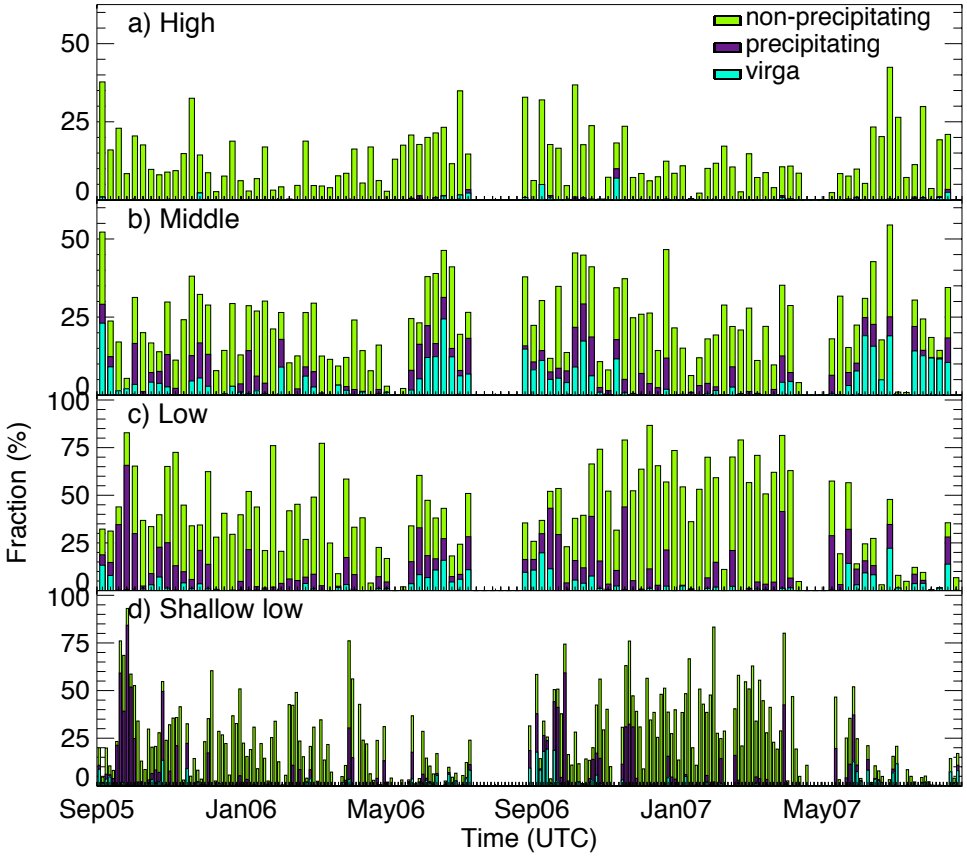

Figure 4–7: Time series of the occurrence of (a) high, (b) middle, (c) low and (d) shallow low clouds on a weekly (a–c) or 3-daily (d) basis. The lower portions of each bar represent the time fraction that cloud was associated with precipitation, reaching (dark blue) or not (light blue) the ground. Note that the gaps around July 2006 and May 2007 are artifacts caused by the lidar's major malfunctions.

Through shorter variations, an annual cycle is obvious for most of the cloud types. First, the high clouds occurrences are maximized during the polar days and minimized during the polar nights, while the opposite applies to the low clouds (especially the shallow ones). Those cycles were expected from the seasonal differences observed in the hydrometeors height coverage. A complete explanation still includes the summertime solar heating, which helps clouds to form higher, and the usual

wintertime polar temperature inversion occurring near the surface, which limits the vertical development of clouds. The middle clouds do not show such annual cycle, concurring with figure 4–5 that shows similar hydrometeor fractions in both summer and winter seasons in the middle troposphere. In fact, figure 4–7b hints toward maxima in both of these seasons. The low clouds also show a maximum just before the first summer, which does not fit in the previously described annual cycle, but it is not repeated in the second year.

From a precipitation perspective, an annual cycle is clearly visible, with clouds preferably precipitating from near the end of spring through mid-fall, but rarely during winter weeks. This is most likely linked to the absence of ice over the channels of the Ellesmere Island (mid-July through early September) and presence of sunlight, providing the needed moisture (through evaporation) and vertical development. There might also be a link to different dominant airmass origins in summer and winter, which could be seen by the wind patterns of the two seasons (see figure 4–3). If the air passes over a mountain range, it loses its moisture content before reaching the observed area, while if it passes over open water, it could increase its moisture content and, thus, its potential to form cloud and/or precipitation.

Nevertheless, most of the time, the precipitating particles evaporated before reaching the ground, thus producing virga. Figure 4–7a shows that high clouds are not often precipitating, but that could be simply an artifact caused by the difficulty to distinguish between cloud ice and falling large ice particles or snow. In fact, this applies to any cloud that is entirely made of ice, like most of winter clouds at all heights, which could have contributed to the observed minimum during winter.

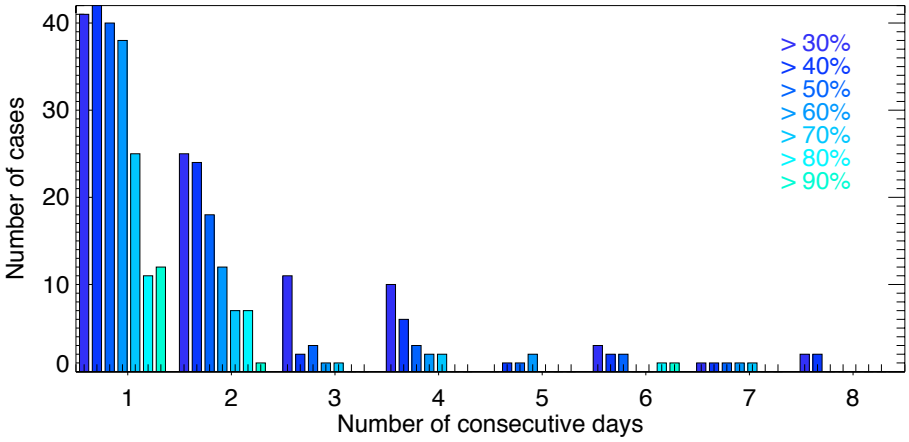

Figure 4–8: Number of consecutive days that the shallow low clouds lasted more than a given fraction of each day. The different colors correspond to different daily thresholds, as shown in the upper right corner.

Figure 4–7d depicts a large variability of the boundary layer cloudiness over short time periods. However, when averaged over a greater time window (even simply a week), that variability disappears. It can be better noticed by looking at the persistence of those cloudy events (see figure 4–8). Most of them lasted only a day or two, while a few isolated cases persisted about a week. As the daily threshold increases, the number of cases decreases, especially for the short lasting ones. This is indicative of the temporal persistence of large-scale or local forcing mechanisms that are responsible for the development of low-level stratus clouds at Eureka.

Additional analysis of these persisting boundary layer stratus clouds was performed in an effort to understand better their formation mechanism, the influence of the strong topography, and what affects their temporal evolution. The horizontal wind direction observed during each possible boundary layer condition (clear, cloudy by a shallow low cloud or by a deep low cloud) is depicted in figure 4–9. First, as

seen in panels (a–c) of figure 4–4, a clear boundary layer is often associated with NE winds at all levels. Moreover, even though there are a few similarities between the two cloudy conditions, differences are also present. For instance, a preference for low-level South winds is shown by both due to the strong topography channelling, but an additional NNW wind channelling seems to prevent the vertical development of the boundary layer cloud. Another main difference is the requirement of North through NE winds aloft to have a confined cloud, which most likely indicates an often clear atmosphere above (as those winds seem to usually mean a clearing).

The turbulence intensity near the boundaries of the persisting shallow low clouds is also investigated (see figure 4–10), using the hourly standard deviation of the MMCR Doppler velocities. It appears that the cloud top is generally more turbulent than the cloud and precipitation bases (see the left panel), although the latter were also experiencing some strong turbulences, due probably to the evaporation of some precipitating water. Moreover, those stratus clouds usually happened at night, and mostly without clouds above them (see the right panel). However, the turbulence experienced near the cloud top during those various situations is quite similar.

It was emphasized in figure 4–2a that hydrometeors are a predominant feature at Eureka almost all year round. However, no information about the overlap of the clouds was given, which can be nicely provided by separating their occurrences into single- and multi-layer systems (see figure 4–11a). It appears that the single-layer system is the preferred one, with a more or less constant occurrence of around 50% in every month. This result is plausible, especially for the nighttime (mostly winter) clouds, as single-layer clouds are often associated with strong large scale forcing,

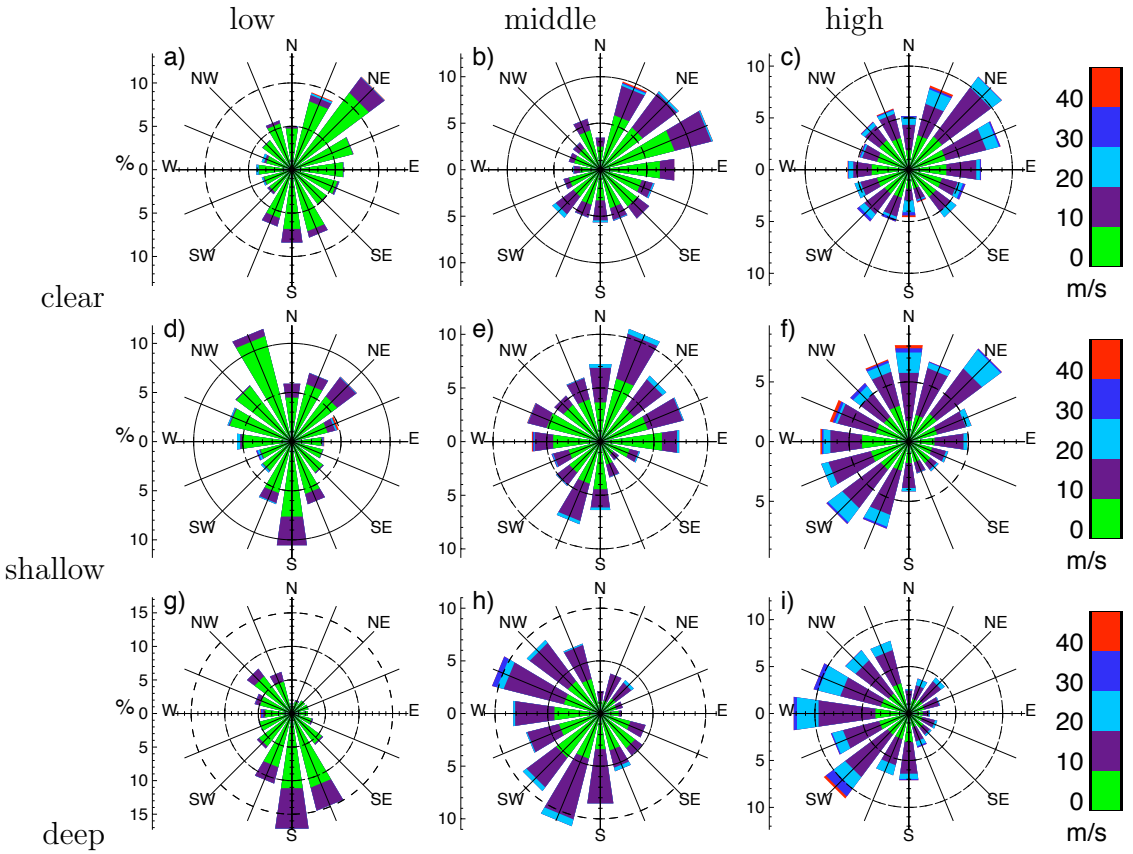

Figure 4–9: Distribution of the wind direction and speed in the low (left), mid (center) and high (right) troposphere, for different boundary layer scenarios: clear boundary layer (a–c), cloud confined in it (d–f) or cloud extending above it (g–i).

and can be maintained by the turbulence created by the radiative cooling happening at their top. In more complicated conditions (like multi-layer clouds), the vertical structure of the atmosphere is more intricate, and radiative heat exchange between the layers offsets the cloud top radiative cooling. As for the daytime (mostly summer) clouds, the explanation is not as simple to find. In fact, it appears that multi-layer systems are more frequently observed during the summer than the winter months.

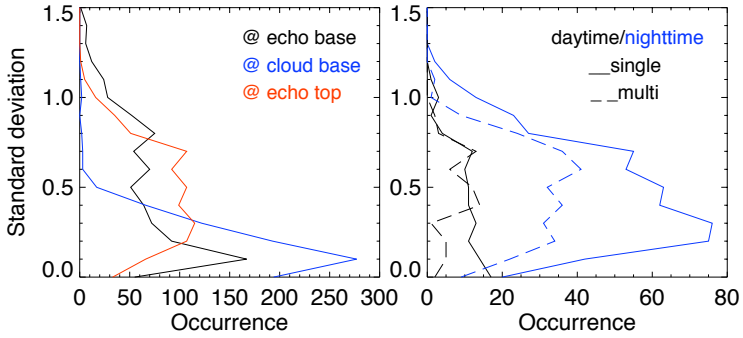

Figure 4–10: Turbulence along the different boundaries of the persisting shallow low clouds: comparison along the radar echo base (black), cloud base (blue) and top (red), in the left panel, and between day (black) and night (blue), along the cloud top, when no other cloud is present above (continuous) or with others (dashed), in the right panel.

The actual number of layers observed in the multi-layer systems was also investigated (see figure 4–11c). In most situations, only two cloud layers are observed (around 15 to 20% of each month), while three layers were observed less than 6% for any month, and greater numbers of layers do not represent more than 1% of cloud conditions in a month. Moreover, each of these systems contributed to the multi-layer curve in the same way, showing the same annual variability than in figure 4–11a.

Additional analysis of the tropospheric horizontal winds retrieved during occurrences of each layer system (clear, single- and multi-layer) can help differentiate them better (see figure 4–12). For instance, it appears that clear skies are dominated by winds coming from around the NE direction at all levels (as seen before in panels (a–c) of figure 4–4), while the cloud systems don't show such a preference. Instead, the single-layer distributions have a peak around the NW direction in the lower levels, displaced toward the West direction higher up, while the multi-layer ones have a

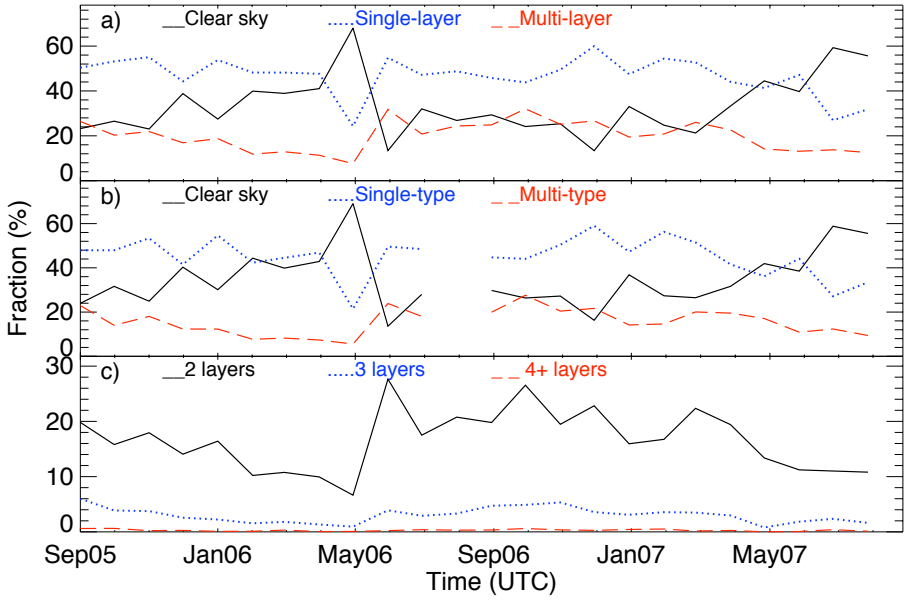

Figure 4–11: Time series of each possible system of cloud layers (a) and types (b) for the two years, on a monthly basis: clear (solid black), single (dotted blue) and multi (dashed red). (c) Decomposition of the multi-layer system time series into the actual number of layers.

preference for the SW direction at all levels (in the boundary layer, it is dragged toward the South due to the channelling, visible for all systems, as noticed before).

From a radiative perspective, the actual combination of cloud types is more relevant than just the number of layers: for example, two cirrus clouds might have a similar effect as only one, but a system composed of a cirrus on top of a low cloud affects the budget quite differently. Thus, clouds systems are divided into *single-type* (if all the profiled layers correspond to the same type) and *multi-type* (if different types were observed together), and their time series are shown in figure 4–11b, with the corresponding clear sky curve. Note that the sum of the three curves does not add to 100% due to the missing data that left some clouds in the unknown class.

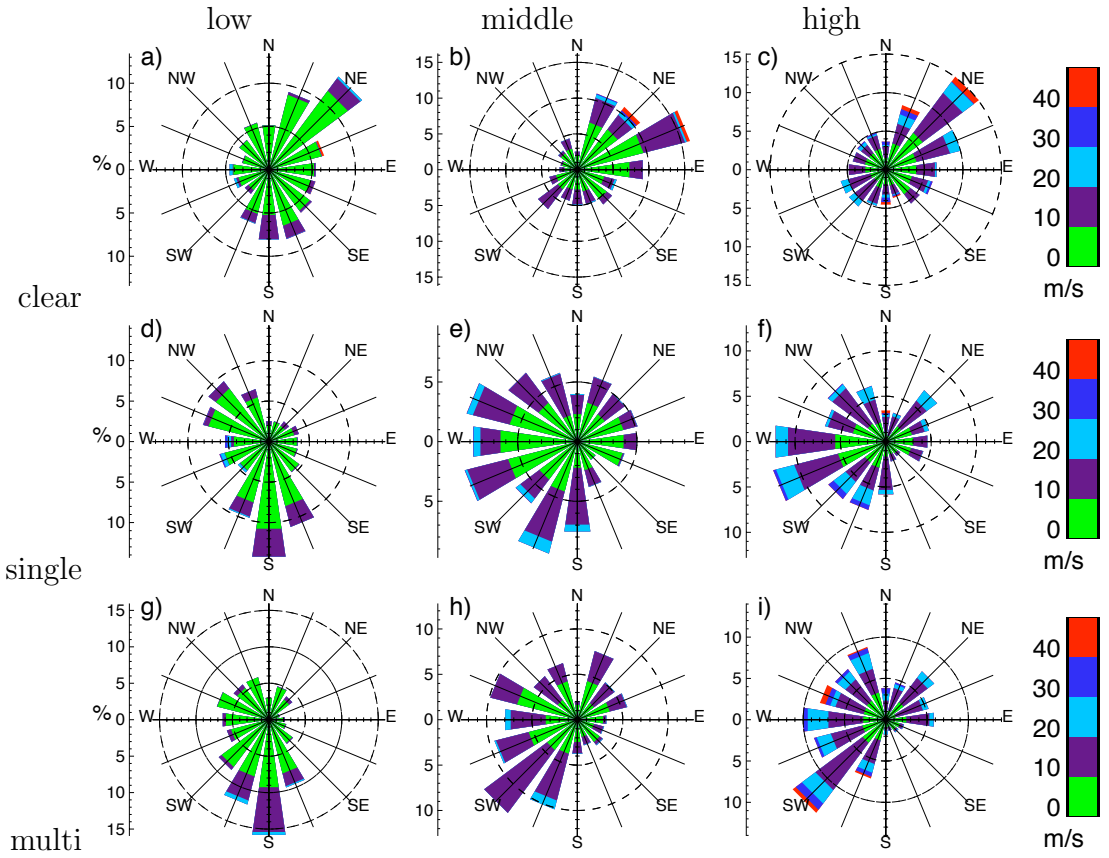

Figure 4–12: Distribution of the wind direction and speed in the low (left), mid (center) and high (right) troposphere, for the different cloud layer systems: clear (a–c), single-layer (d–f) or multi-layer (g–i) conditions.

Nonetheless, the same annual cycle is depicted, despite some slight differences in the numbers, demonstrating that the muti-layer systems are usually also multi-types.

A further investigation of the cloud combinations is provided in figure 4–13, representing all the possible combinations of the three main types on a monthly basis, including the single-layer cases. Panel (b) shows that, in fact, a few of the multi-layer systems were in fact single-type, mostly winter's low clouds (usually a shallow low cloud with an extending one) and summer's middle clouds. Otherwise,

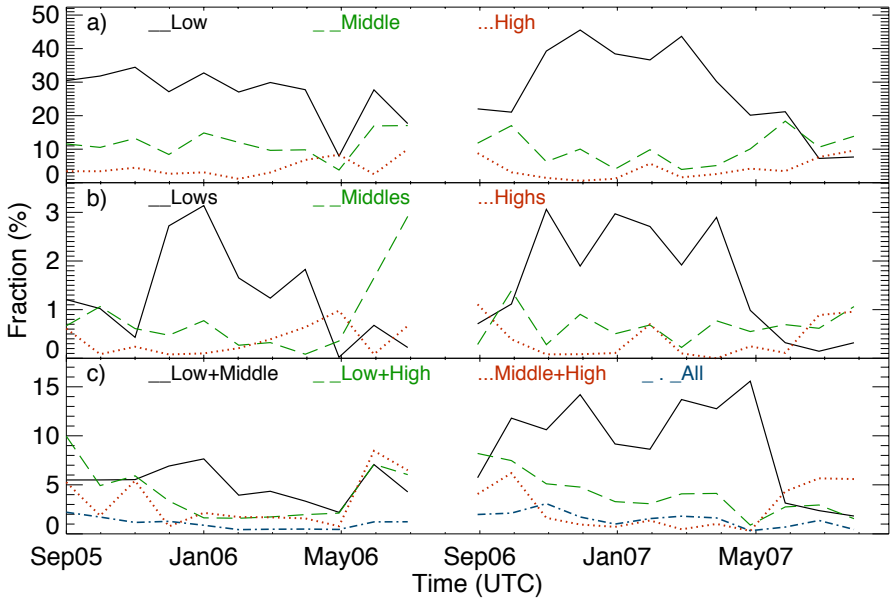

Figure 4–13: Time series of the different combinations of cloud types occurring on a monthly basis during the whole time period. From top to bottom: single-layer cases, multi-layer cases that are single-type, actual combinations of different types.

they were dominated by the combination of low (usually the shallow ones) with middle clouds, especially during the second year (see panel (c)). However, as noticed previously, clouds are able to get higher more often around the summer seasons and, therefore, combinations including high clouds were peaking during those periods. Finally, all types of clouds were observed together from time to time all year round, but mostly during the fall seasons.

As for the single-layer cases (see panel (a)), they were usually caused by low clouds, except maybe during summertime when the middle and high single-layer cloud occurrences both peaked. Furthermore, as noticed in figure 4–11, the single-layer systems happened more often than the multi-layer ones, especially during the winters. Moreover, during the yearly minima in cloudiness (May 2006 and July

2007), the low clouds experienced a local minimum, while the high (and middle for the latter case) clouds were maximizing.

Figure 4–14 depicts statistics about the cloud boundaries for each type, in different ways. Note that, when a profile contained more than one layer of a given type, only the deepest cloud was considered since it is the one that should have affected the most the radiation budget. The left panels indicate that the clouds boundaries were quite variable, even on a weekly basis, especially the tops. For the high clouds however, those variations were following similar patterns for both the bases and tops, creating a narrow distribution of their depths (see the upper-right panel) and allowing their hourly-averaged boundary curves to be quite similar (see the upper-mid panel). The same situation was observed for the boundary layer clouds (not shown here), but not for the low clouds extending above it, allowing for the sharp peak in the low clouds hourly-depth distribution (see the lower-right panel), even though it spreads to great depth too.

Furthermore, it is noticeable that the high and low clouds formed higher during the summer, while the middle clouds had their averaged bases between 3 and 4 km all year round, as seen previously in figure 4–5. Finally, most of the time, clouds are quite shallow, with hourly-depths of less than 1 km, although some of them managed to extend deeper and to last long enough to create greater hourly-depths, especially the middle and low clouds which were observed to be as deep as 6 km and even more. That preference for shallow systems imply that stratus-like clouds last longer than the deeper cumulus-like clouds, especially in the low levels, creating more shallow hourly-depths.

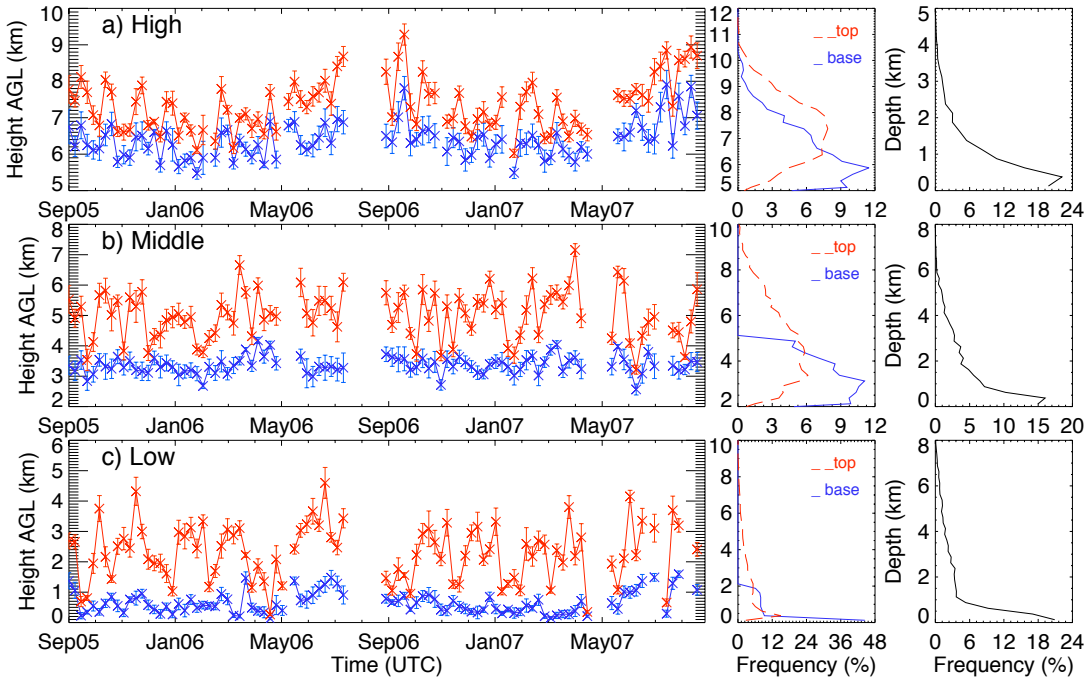

Figure 4–14: Time series of the weekly boundary heights (left panels) and distribution of the hourly boundary heights (middle panels) and depths (right panels) for high (a), middle (b) and low (c) clouds.

4.2 Hydrometeor Phase

Since the atmospheric water has a different impact on the radiation budget depending on its state, the hydrometeor phase needs to be determined properly. To ensure that our classification (described in section 3.2) gives consistent results, some histograms are provided and discussed here, starting with the temperature distribution within each phase composition, obtained after applying the whole algorithm, shown in figure 4–15a. The discontinuities observed at −40 and 0℃ are due to the hard thresholds of the classification process (solid below −40℃ and liquid above 0℃).

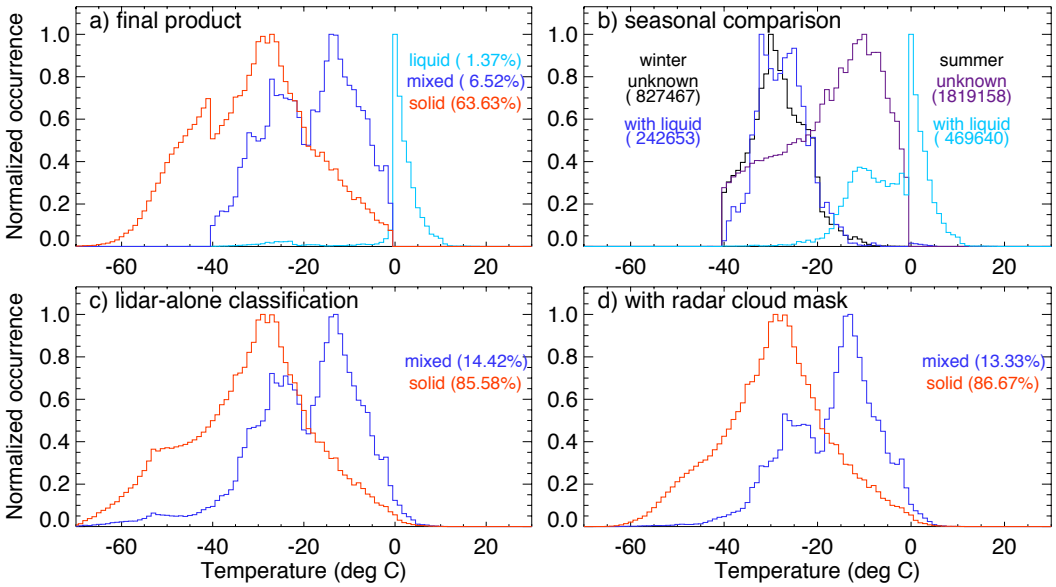

Figure 4–15: Distribution of the soundings interpolated temperatures among the hydrometeor phases, as obtained from the whole algorithm for the two years (a) or comparing the winter and summer seasons (b), as well as from only the criteria shown in figure 3–3 (c) and applying a radar cloud mask (d). The numbers in brackets represent the fraction of sampled volumes (except in (b) where it is the actual number of pixels) found with each composition, within the temperatures shown here.

A further classification of the unknown class, as well as a better recognition of the liquid-only volumes from the mixed-phase, would most likely remove those artifacts.

Another interesting feature in that histogram is the double-peak signature of the mixed-phase curve, around −15 and −25℃. This could also have been caused by the non-classified hydrometeors (all found between −40 and 0℃) and the inclusion of some liquid-only volumes into the mixed-phase (most likely at supercooled temperatures closer to 0℃). Part of the explanation might also reside in the seasonal differences, as depicted in panel (b). As the summertime experiences more often liquid particles, and in greater concentrations, the resulting attenuation might have

prevented most of the classification aloft, where hydrometeors encountered colder temperatures. On the contrary, during wintertime, most of the hydrometeors are found at temperatures below −20°C, without much liquid, allowing for a better sampling of the supercooled liquid.

A detailed look into the phase classification obtained from the lidar measurements alone (see figure 4–15c–d) can help make sure that the temperature thresholds are reasonable and the lidar-based classification is reliable. No liquid-only curve is shown, since either the temperature or radar measurements are needed to retrieve it. Panel (c) shows the temperature distributions among the phase compositions obtained from the lidar measurements only (using simply the criteria indicated in figure 3–3). A weak peak below −50°C is visible in both curves. However, they disappeared in panel (d), where only the results found inside radar echoes are considered (using a basic cloud mask obtained from the radar measurements), demonstrating that they were caused by the lidar speckled echoes found at high heights.

As in panel (a), the mixed-phase curve is showing two peaks, which supports the explanations given above. More importantly, it should be noticed that the solid-only curve extends above the melting level, while the mixed-phase volumes are sometimes found at temperatures colder than −40°C, even after the removal of speckled noise. Nevertheless, those represent only a small fraction of the hydrometeors sampled by both sensors, respectively 0.5 and 0.2% (or 0.6 and 1.3% of their respective curves). Thus, according to the lidar criteria, the temperature thresholds used here are quite reasonable, affecting less than 1% of the hydrometeors sampled by both sensors, which could even be simply caused by the temperature interpolation.

Similarly, figure 4–16 depicts the distribution of other observables values among the different phases compositions, obtained after the whole classification. Panel (a) shows it for the radar reflectivity factor. The high reflectivity values for the liquid return are caused by large raindrops, and the observed peak is due to radar receiver saturation. The distribution of the mixed-phase pixels is quite similar to the all-solid curve, emphasizing the domination of the radar echoes by the solid phase (ice particles), although it extends to lower reflectivity values, down to the all-liquid curve in fact, which might be a sign of misclassification or simply that the supercooled liquid droplets are in higher concentration. Finally, the slight discontinuities at -60 and -50 dBZ are most likely caused by the radar and the multiple operational modes that are used to detect all hydrometeors in all levels of the atmosphere, although the algorithms might have contributed as well.

Panel (b) presents the Doppler velocities associated with each phase compositions. The spike in the liquid distribution is caused by the threshold used at 2.5 m/s and, again, a further classification of the remaining unknown pixels would most likely eliminate it. The rarely observed highly negative (upward) velocities are caused by the folding of some fast falling liquid hydrometeors. That graph also shows that the radar signal is dominated by the crystals present in the volume, as the two other curves are quite similar, at small falling velocities. Despite those similarities, it is important to note the slight shift of the mixed-phase returns distribution toward upward motions, consistent with all existing theories for the production of supercooled liquid that require the presence of updrafts.

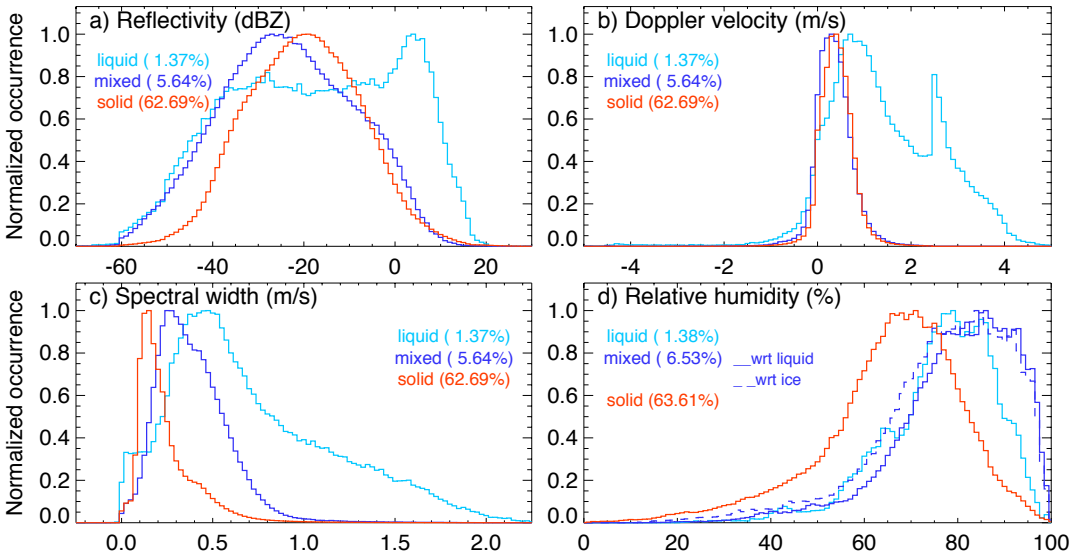

Figure 4–16: Distribution of the hydrometeor phases with the radar reflectivity (a), Doppler velocity (b) and spectral width (c) and among the soundings interpolated relative humidity (d). The numbers in brackets represent the fraction of sampled volumes found with each composition, within the limits of the x-axis.

Panel (c) displays the spectral width distributions. The liquid-only curve has two peaks: one for the precipitating particles (well defined at high width) and one for the cloud droplets (hinted at near-zero width). This is explained by the fact that liquid precipitation has drops of various sizes and a consequently larger Doppler spectrum, while the cloud droplets are all small and follow mostly the atmospheric winds, creating a narrow Doppler spectrum. The two other curves peak at intermediate values: the solid-only one has mostly low widths, while the mixed-phase one is characterized by larger widths (but still usually smaller than the liquid precipitation). These results are also easily explained: solid particles are normally characterized by similar fall velocities (as seen in panel (b)), providing a narrow Doppler spectrum

for the solid-only pixels, while the droplets usually have smaller velocities, widening the mixed-phase volumes Doppler spectra.

Panel (d) depicts the phase compositions as a function of the relative humidity (computed from the rawinsondes retrieved pressure, temperature and dew point temperature), with respect to liquid or ice, depending on the composition considered. It clearly shows that the liquid phase needs higher humidity content to form than the solid particles. Furthermore, the mixed-phase volumes usually require even higher humidity, indicating the need of saturation with respect to liquid in order to sustain the liquid particles despite the presence of the solid phase. On its other side, however, that curve gets quite close to the liquid-only distribution, which hints again toward a double-peak signature: one around 90% and the other near 65%, the latter being most likely caused by rain drops, which often fall in a sub-saturated environment.

Finally, the percentages shown in brackets in both figures 4–15 and 4–16 represent the number of volumes found with the corresponding phase composition, over the total number of those classified as containing hydrometeors. Notice that the percentages in a given panel are not adding to 100% (except in panels (c–d) of figure 4–15, since only the volumes sampled by the lidar are considered), the difference representing the fraction of unknown hydrometeors. Moreover, the percentages are not the same in all plots, due to the limits considered for the computation of the curves and to differences in the number of volumes well-sampled by each instruments.

Despite its problems, the hydrometeor classification is reasonable and can be used to draw some conclusions. Panels (a–c) of figure 4–17 show the distribution with height of the monthly-averaged occurrence of each hydrometeor class. As in

figure 4–15a, solid hydrometeors are found alone at heights where the temperature is below −40°C, while only liquid is observed at temperatures above the freezing point. Between these two temperature values, the majority of the radar-lidar detections are in their solid phase only, while supercooled liquid is frequently found, especially at temperatures above −20°C. Nevertheless, many hydrometeors are still in the unknown class, mostly during the summer, when more low-level liquid is present to attenuate efficiently the lidar signal. Thus, it is quite possible, as mentioned above, that liquid hydrometeors were present aloft (at colder temperatures), but could not be identified.

Figure 4–17d shows the fraction of good observation time within each month that liquid hydrometeors were observed, with or without the presence of solid particles within the same analyzed volume. As in previous studies (Intrieri et al., 2002; Shupe et al., 2006), those were detected all year round, following a similar cycle as the cloud occurrences: maximized in summertime, closely after reaching its minimum. That cycle is related to the cloud coverage variability, as no liquid is observed without cloud presence. Nevertheless, the lower numbers during the winter might also be caused by the colder temperatures, preventing the formation of liquid.

Figure 4–18 provides the means to look at the height dependence for each phase composition in more details. In fact, it shows the mean and standard deviation of the daily fraction of sampled hydrometeors that contained or not liquid or that stayed unclassified, comparing the winter and summer results at every resolved height. The end of the curves indicates the highest height for which days with hydrometeors there were in sufficient numbers to provide a reliable result (the near-zero fractions

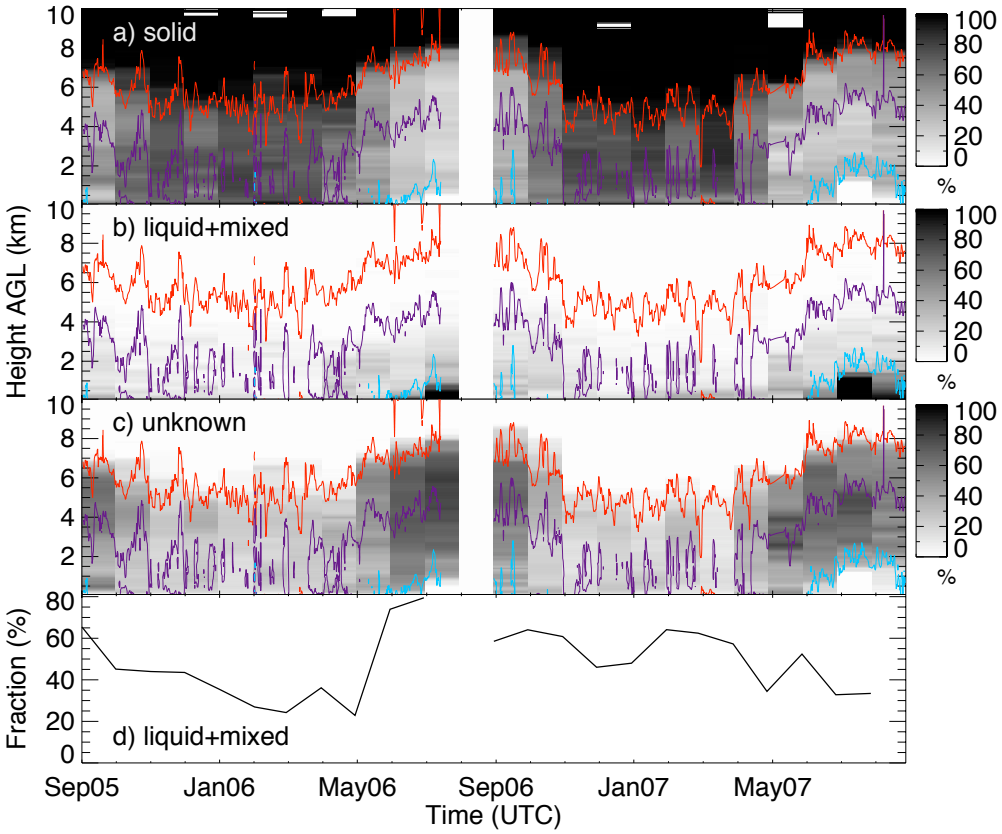

Figure 4–17: Distribution with height of the monthly fraction of hydrometeors found in (a) solid, (b) liquid (alone or with ice) and (c) unknown phase, and (d) fraction of time that liquid hydrometeors were detected, in any amount and combination. The lines in a–c represent the −40, −20 and 0°C isotherms.

in figure 4–5). Notice that a good portion of all the curves for a given season have no standard deviation, since the hydrometeors above that height were always experiencing a temperature below −40°C, forcing the solid classification for all of them.

In both seasons, very little liquid was detected above 3 km. During summer, this can still be explained by the strong attenuation experienced, as emphasized here

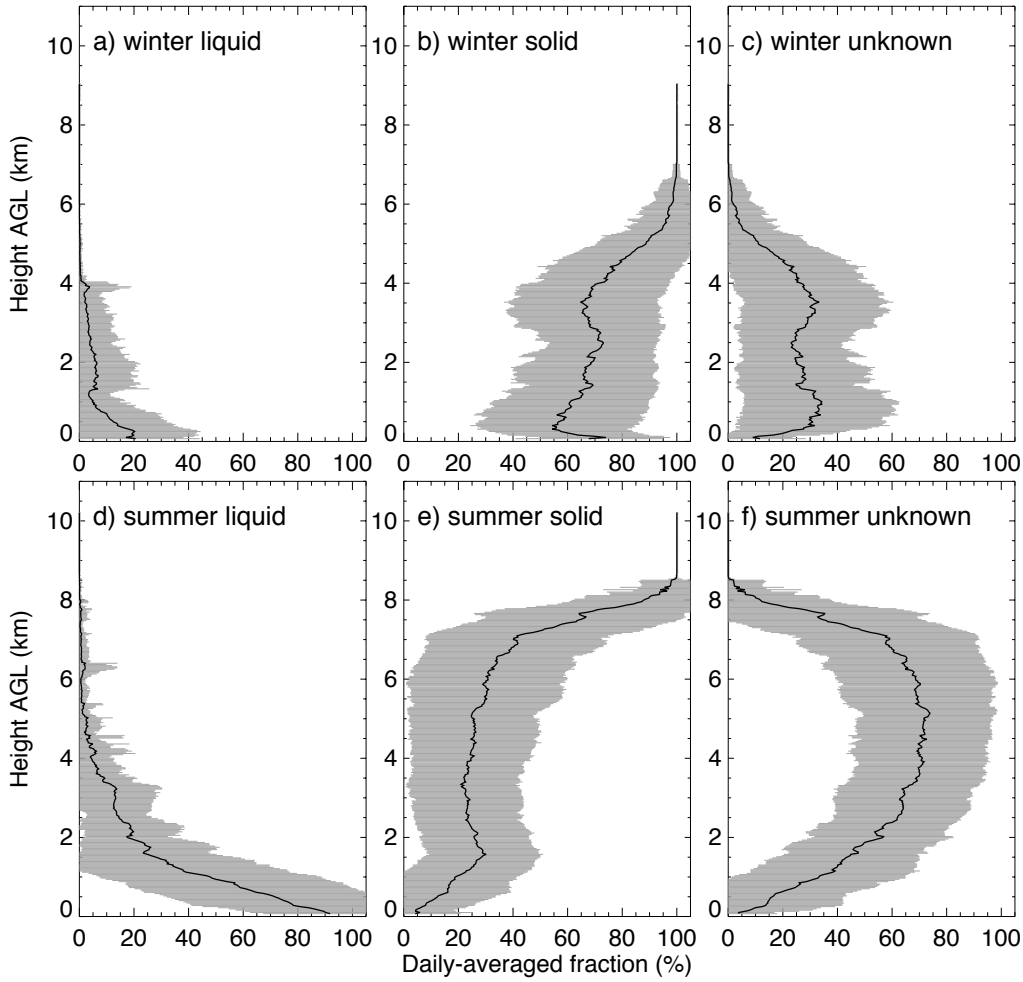

Figure 4–18: Mean (solid lines) and standard deviation (grey shading) of the daily fractions of hydrometeors found containing liquid (left), only solid (center) or unknown (right) phases, as computed at every height, for the winter (a–c) and summer (d–f) months. The end of the solid curve indicates that hydrometeors were not found in sufficient numbers to return a number here (corresponding to the height of near-zero fraction in figure 4–5).

by the high daily fractions of low-level liquid (especially near the surface) and high-level unknown (everywhere, but mostly between 2 and 7 km). On the contrary, the wintertime seems to really be dominated by solid particles alone, as shown by their

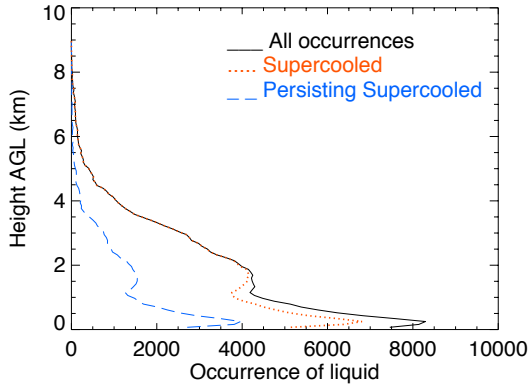

Figure 4–19: Height distribution of the hourly occurrences of volumes containing liquid: all occurrences (solid black), only the supercooled occurrences (dotted red), and those supercooled that persisted more than 50% of an hour (dashed blue).

high daily fractions at all heights. Finally, solid hydrometeors can be found near the surface all year round, although there is very little during the summer days.

Another way to look at the liquid occurrences (with or without the presence of solid in the same sampled volume) is to investigate them within hourly volumes, and isolate those that were supercooled and persisted at least half of an hour. The first restriction removes the hydrometeors classified as liquid due only to their temperature, while the second takes care of the volumes that happened to contain liquid, by chance. The resulting height distribution is depicted with 90-m bins in figure 4–19, which includes the effects of adding each restriction. The former removes only a few occurrences in the first 2 km of the troposphere, while both together leave less than half of the occurrences at every height. This indicates that, when liquid forms, it tends to disappear quickly, or changes height at least.

Nevertheless, many occurrences are still considered here, with most of them happening in the first kilometer above the surface. In fact, as discussed previously,

it is quite likely there were more of them aloft that could not be properly sampled by the lidar, especially during the summertime. Moreover, there seems to be a dip around 1 km high in all curves. The same discussion could still hold here, but more is required to explain an actual dip, such as the observed dominance of the winter shallow low clouds, which were often mixed-phase around that height. Lastly, notice that supercooled liquid was detected close to the surface, although not as often as just above those few first gates. Those lowest occurrences must have been caused by either low cloud bases, sub-zero liquid precipitation, or even above freezing precipitation in a hourly volume that had a mean temperature below 0℃.

These occurrences have been analyzed in comparison to the hourly occurrences of volumes containing only solid hydrometeors, that persisted more than half of an hour (as for the liquid). Moreover, every volume with a mean temperature below −40℃ was removed, to avoid introducing any bias due to the simple temperature classification (as previously for the liquid). The distribution of some observables associated with those two sets of occurrences are presented in figures 4–20 and 4–21.

When comparing panels (a–c) of figures 4–20 and 4–16, it is noticeable that the former are missing part of the high reflectivity and high velocity peaks, indicating the supercooled persisting liquid occurrences are mostly composed of cloud droplets, as opposed to precipitation, while having moderate spectral width, hinting the presence of ice crystals with most of them. Furthermore, the liquid phase seems to require more turbulence than the solid phase in order to last longer, as demonstrated by both panels (c) and (d) of figure 4–20.

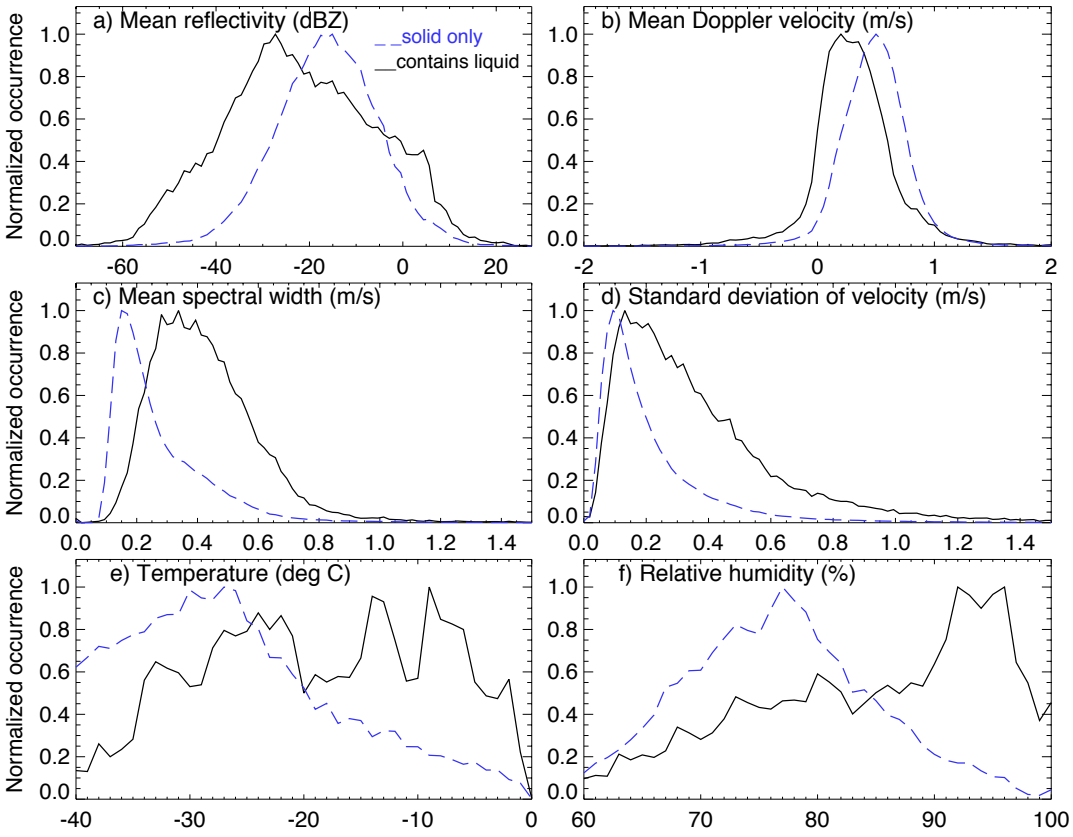

Figure 4–20: Comparison of the hourly mean of the radar (a) reflectivity, (b) Doppler velocity and (c) spectral width, as well as (d) the standard deviation of the Doppler velocity over an hour and the soundings retrieved (e) temperature and (f) relative humidity, within volumes containing (solid black) or not (dashed blue) supercooled liquid particles more than 50% of an hour.

Panel (e) shows that supercooled liquid can persist at various temperatures, without any real preference, while solid seems to rather form alone at temperatures below −20°C. Although their absence at lower temperatures might be simply caused by the summer attenuation, it can be argued that they occur more easily at the colder temperatures since it gets harder for the liquid to form and persist as the temperature decreases. Lastly, as seen previously in figure 4–16d, liquid occurrences

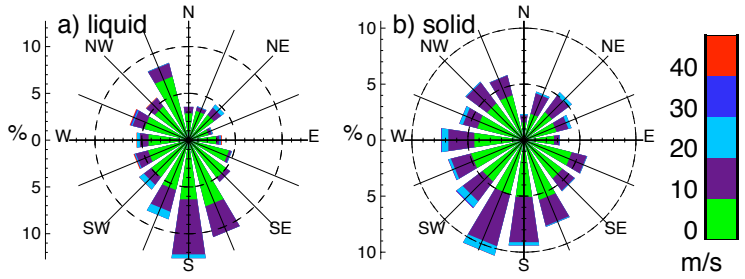

Figure 4–21: Comparison of the wind speed and direction within hourly volumes containing (a) or not (b) liquid particles more than 50% of an hour.

are normally associated with higher relative humidity than the solid-only volumes (see figure 4–20f): above 90% for the former, as opposed to usually less than 80% for the latter. The transition seems to happen around the 90% level, where the relative fraction of both phases takes a sharp turn. In fact, below 95%, most of the persisting hydrometeors are solid (it is almost all of them below 90%), while both phases can easily coexist at higher humidity.

Finally, figure 4–21 compares the horizontal winds direction and speed associated with both phases. As observed previously, it seems that hydrometeor formation is prevented by winds coming from around the NE. Furthermore, supercooled liquid successfully persists mostly with the NNW and southern winds (see panel (a)), which are the directions that follow the main water bodies near Eureka, thus allowing the air to increase its moisture content when they are unfrozen. Although that channelling is not as well marked for the solid-only occurrences (see panel (b), directions with a western component are also well represented), the contrast is not important enough, and more cases are needed to link the presence of supercooled liquid to particular wind directions.

Chapter 5
Potential Utility for Satellite Instrumentation

The US National Aeronautics and Space Administration (NASA) launched two satellites in 2006, CloudSat (Cloud Satellite) and CALIPSO (Cloud-Aerosol Lidar and Infrared Pathfinder Satellite Observation), respectively flying the first space-borne cloud radar (the *Cloud Profiling Radar* (CPR), Stephens et al., 2002) and dual-wavelength polarized lidar (the *Cloud-Aerosol LIdar with Orthogonal Polarization* (CALIOP), Winker et al., 2007). They both joined the A-Train (satellites orbiting in formation to observe the troposphere, see figure 5–1) in June 2006, transmitting their first measurements soon after, about 10 months after Eureka's MMCR and AHSRL became operational.

During this project, the data from Eureka's MMCR were used to evaluate their potential to validate CloudSat's CPR. Although not done here, a similar study could be carried out for CALIOP using the AHSRL measurements. Moreover, the success

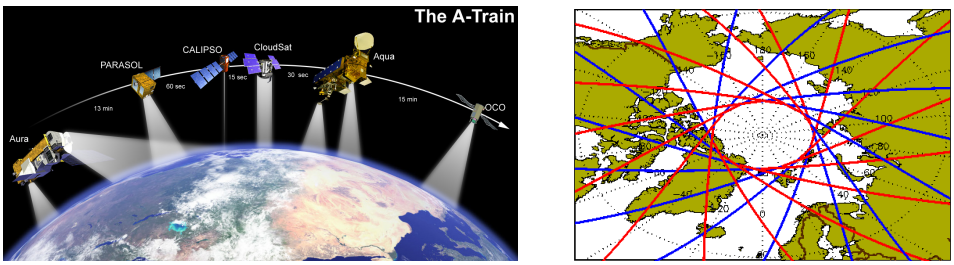

Figure 5–1: The A-Train satellites, with CloudSat and CALIPSO in the middle, (left) and their numerous swaths over the Arctic region on March 02, 2007 (right).

of the A-Train mission so far encourages the European Space Agency to prepare the next space-borne atmospheric observatory, the Earth Clouds, Aerosols and Radiation Explorer (EarthCARE) satellite, which will be a single platform containing, among other instruments, a cloud radar and an HSRL, planned to be launched in 2013. Those will be even more similar to Eureka's instruments and the knowledge learned from this project, as well as others combining similar instruments, could be applied to the development of synergetic retrievals for that mission, such as a precipitation or phase recognition algorithm.

5.1 CloudSat Evaluation Using Eureka Measurements

The CPR profiles clouds in a similar way as the MMCR, sending a signal at a given frequency, always vertically, and analyzing the part that comes back to its antenna. However, the CPR is pointing downward, instead of straight up, causing the returned signal to be affected by the high reflectivity of the surface, especially in the lowest kilometre of the atmosphere. The degree of contamination depends on the type of surface (land, ocean, ice...) and the attenuation encountered by the signal, which is more important for the CPR due to its higher frequency (94 GHz, W band), as shown in figure 5–2. Moreover, the shorter wavelength of the CPR brings non-Rayleigh effects in its measurements for smaller particles than the MMCR.

Another obvious difference is the orbiting aspect of the CPR, allowing it to sense clouds globally (or almost), but also requiring a greater distance from the sampled particles (around 700 km above them). Furthermore, its sampled column is always changing, dictated by the satellite path (as opposed to the clouds movement for the MMCR), which is moving at a speed of 7 km/s. Thus, even though the CPR beam

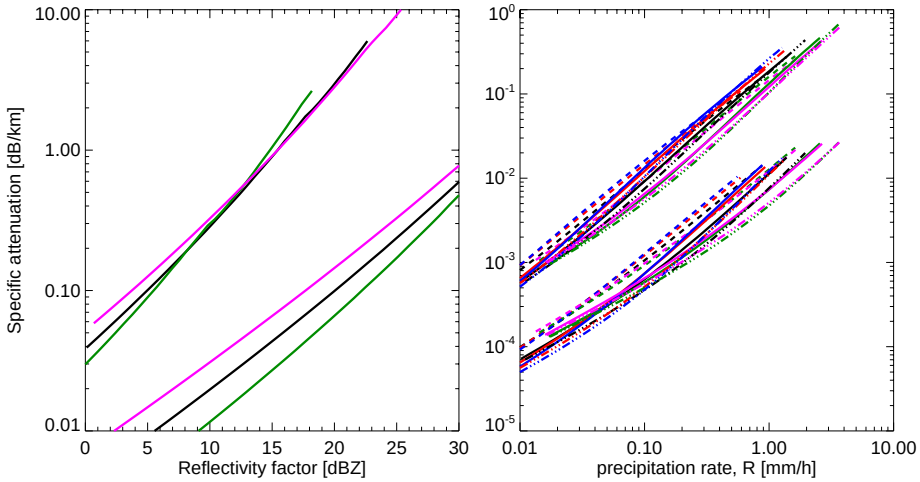

Figure 5–2: One-way specific attenuation computed under rain (left) or snow (right) conditions, for two frequencies: 94 GHz (W band, like the CPR, upper sets of curves) and 35 GHz (K_a band, like the MMCR, lower sets of curves). Each curve in a group represents the result obtained from a different size distribution (courtesy of W. Szyrmer from McGill University).

width (half-width less than 0.12°) and time resolution (integration time of 0.16 s) are smaller, the resulting field of view provides coarser resolutions than the MMCR, with an oblong shape of approximately 1.7 km along-track and 1.4 km across (at the ground), mostly due to its high altitude. As a comparison, the MMCR time resolution can be converted to a 100-m "along-track" resolution, assuming a mean horizontal wind of 10 m/s. The CPR has also a much coarser vertical resolution (around 240 m), due to its greater pulse width (3.3 μs), although it easily covers the whole Arctic troposphere, and even more, thanks to its low sampling rate (4300 Hz).

CloudSat is less sensitive than the MMCR (expected from −29 to −26 dBZ throughout its mission), due mostly to its high altitude and space constraints. Nevertheless, Stephens et al. (2002) estimated that it should detect most clouds that

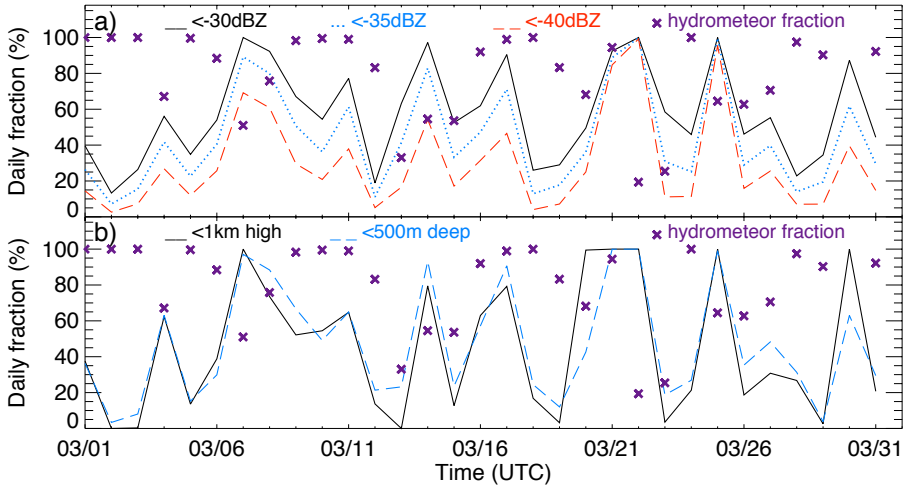

Figure 5–3: Daily fraction of (a) MMCR echoes found below a given threshold (−30, −35 or −40 dBZ, respectively in solid black, dotted blue and dashed red) and of (b) low or shallow clouds (solid black and dashed blue respectively), during the month of March 2007. In each panel, the crosses represent the fraction of each day that experienced hydrometeors.

have a significant impact on the radiative budget of the atmosphere, while stressing that the missed clouds impact must be assessed. Using the MMCR higher sensitivity, a first estimate of the amount of hydrometeors not detected can be obtained. For instance, the solid black line in figure 5–3a indicates the fraction of echoes that were below −30 dBZ during each day of March 2007, showing that some days experienced predominantly low reflectivity clouds. However, those events were often even less reflective, as noticed when a lower reflectivity threshold is used (see the other lines in figure 5–3a), and usually lasted only over a short time period in shallow and/or low clouds (see figure 5–3b) that are hard to detect by the CPR.

CloudSat repeats its orbit only every 16 days, within 20 km of the previous tracks. Nevertheless, thanks to its Arctic location, the Eureka region gets profiled

more often (see the right panel of figure 5–1), although the tropospheric columns profiled by each radar will rarely be co-located, and any comparison between their measurements and derived results must be done carefully. First, an area around the ground-based instrument must be selected, as well as a time frame. Here, a maximum distance of 100 km from the ØPAL was chosen, with profiles taken during March 2007, providing more than 20 overpasses, despite four days where CloudSat was in standby. Many of them were taken twice daily, one in the morning during descent and the second in the afternoon during ascent, but rarely on following days, thus representing 14 profiled days. Within those overpasses, the shortest distance between the CPR and MMCR beams varied from less than 1 km to more than 60 km, with a mean closest distance of approximately 30 km.

Then, relevant profiles should be identified and brought to similar resolutions and sensitivity (usually, only the ground-based instrument measurements are affected). While doing so, the partial beam filling issue related to the volumes of the CPR is investigated. Figure 5–4a shows that, according to the MMCR measurements, the large majority of CPR volumes are completely filled by hydrometeors during March 2007, while only near the cloud boundaries that partial beam filling effects were found for the CPR (as seen in the example shown in panel (b)).

Further information can be obtained by comparing the measurements taken by each instrument over corresponding periods, keeping their original resolutions. To find such periods, one must first know the length of the path taken by CloudSat that falls within 100 km of ØPAL. Then, assuming that the hydrometeors were uniformly advected above the MMCR by a 10-m/s wind (more or less in a direction opposite

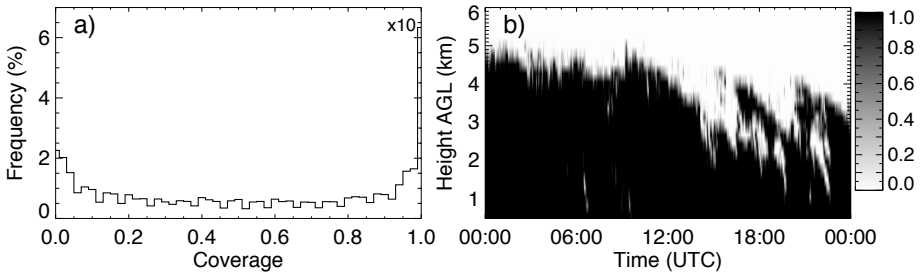

Figure 5–4: Coverage of CPR-like volumes by MMCR volumes having a reflectivity greater than −30 dBZ during March 2007 (a) and its time-height plot for March 2, 2007 (b).

to the CPR trajectory), a corresponding MMCR time period can be found, with the middle time taken as the time of the closest CPR approach to the Eureka site.

Two examples are further discussed here. First, the descending overpass of March 5, 2007 is depicted in figure 5–5, along with the corresponding measurements taken by both radars. Even though the CPR beam got relatively close to ØPAL (almost 30 km), the two reflectivity plots show great differences: a quasi-complete loss of the lower layer by the CPR, while the upper one has a more variable height and is not as well sampled. A possible explanation is an actual difference in the atmospheric situation, as indicated by the associated MODIS image (not shown here). Nevertheless, it is possible that surface contamination and the subsequent removal of too much signal have contributed to the loss of the low-level layer, while the lower sensitivity of the CPR might have prevented the proper detection of the upper layer, as shown by the bluer colors along its MMCR boundaries.

Additional statistics of the measurements obtained by the two cloud radars are shown in figure 5–6. Panel (a) compares the distribution of their reflectivity factors, showing that the MMCR is characterized by a dual distribution, with a peak

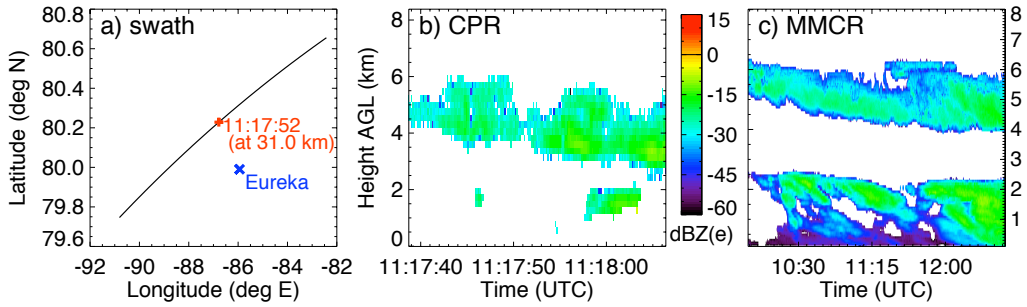

Figure 5–5: Trajectory followed by CloudSat in Eureka's surroundings on the morning of March 5, 2007 (a), along with the corresponding reflectivity measurements taken by the CPR (b) and MMCR (c).

lower than −30 dBZ that was mostly missed by the CPR due to its low sensitivity. Nevertheless, the higher reflectivity factors are similarly represented by both sensors, showing that the CPR and MMCR are in good agreement.

Panel (b) analyzes the height distribution of the reflectivity, once it was averaged over the considered period. It clearly indicates that the CPR did detected two layers, although the lower one was partially masked by surface contamination. It also shows that they were both sensed lower by the CPR, with the upper layer reaching greater reflectivity than at Eureka, which might be simply due to spatial variations in the cloud cover, since both curves agree within one standard deviation. Finally, the fraction of hydrometeors detected as a function of height during the whole period by each radar show similar results (see panel (c)), emphasizing the lowering of layers detection and the partially miss of the lower layer.

The second example was taken during the descending overpass of March 2, 2007 (see the satellite trajectory and corresponding radars reflectivity measurements in figure 5–7). Although the CPR beam stayed further than 50 km from ØPAL, the

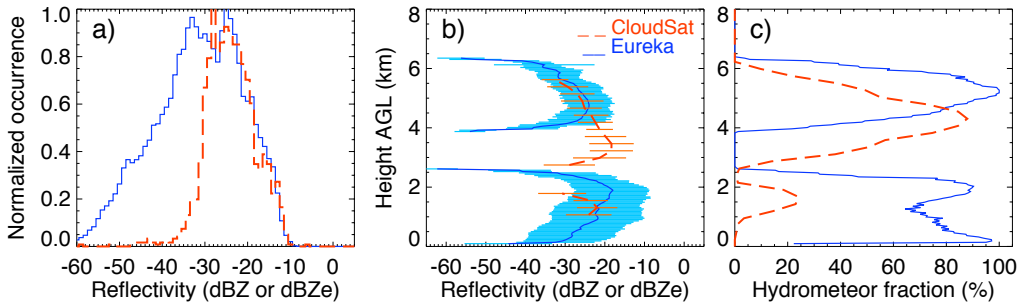

Figure 5–6: Analysis of the CPR (dashed red) and MMCR (solid blue) measurements obtained during the descending overpass of March 5, 2007: distribution of reflectivity as measured at every pixels (a), reflectivity averaged over the whole period at each sampled height, with the associated standard deviations (b), and the fraction of the whole period that hydrometeors were observed at every sampled height (c).

two reflectivity time series look more alike than the first case: both radar images have a top around 4 to 5 km, slightly descending with time, and reflectivity increasing downward with similar values (except for some low-level redish values for the CPR, which might be due to an incomplete surface signal removal). Some minor differences can still be observed (like a better defined echo top and diagonal stripes in the MMCR image), but they are most likely due only to the better resolution and sensitivity of the MMCR, since this case was quite homogeneous in space (shown by MODIS images found on the NASA's website, not included here).

Additional analysis is shown in figure 5–8. Panel (a) includes the distribution of the reflectivity detected at every considered pixels for each radar, indicating a remarkable agreement. In fact, they seem to be off by only 1 dB, despite other minor differences that can easily be explained by the instruments' limitations. The MMCR tail extending to -50 dBZ could not be retrieved by the CPR due to its lower sensitivity, while some remaining surface contamination have more likely added high

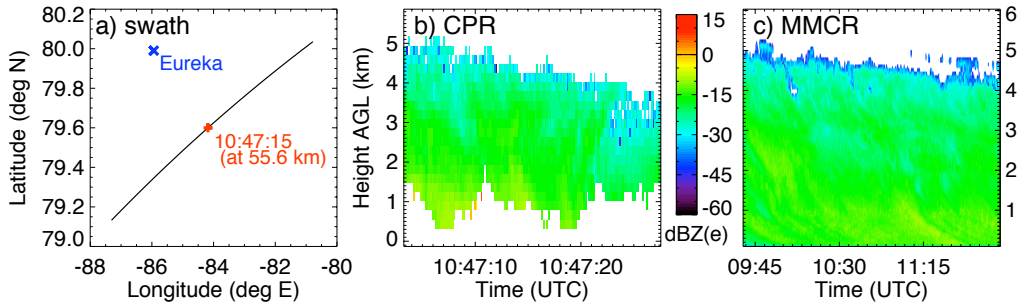

Figure 5–7: Same as in figure 5–5, but for the descending overpass of March 2, 2007.

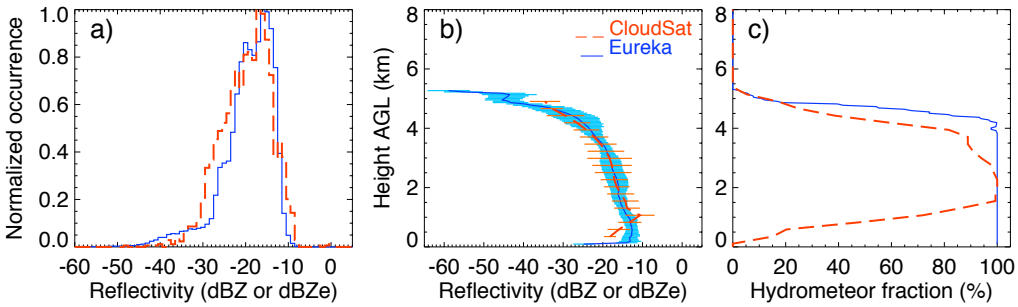

Figure 5–8: Same as in figure 5–6, but for the descending overpass of March 2, 2007.

values to the CPR plot (mostly found at the lowest heights). Finally, the CPR curve shows more intermediate values to the left of the peak that could be explained by the bigger size of the sampled volumes since they were mostly found near the top of the echo layer.

Similar observations can be made from the comparison of the averaged reflectivity profile of each radar (see panel (b)). The agreement is quite good between 1.5 and 4.5 km, with greater CPR values just below and above those two limits, respectively, as mentioned previously. At even lower heights however, the CPR detected smaller reflectivity on the average, but only a few CPR observations were left at those heights after the surface contamination was removed. Finally, the fraction of

time hydrometeors were observed at every height by each sensor (see panel (c)) also indicates a good agreement in the middle of the layer. As it was apparent in the first case, surface echo contamination prevents detections in the lower kilometre, while the MMCR high sensitivity allowed it to detect better the upper part, although some spatial differences might also have played a role here.

From those simple examples, a validation of CloudSat radar seems possible using the Eureka's MMCR, even though there are differences between the instruments if certain conditions are met. First, a case with hydrometeors in their solid phase is preferred to avoid any strong attenuation affecting mostly the CPR. Second, a high degree of homogeneity in space and time is needed to remove most of the non-colocation effects. Third, an important part of the observed hydrometeors should be higher than 1 km above the ground to carry out the comparison without worrying about a remaining surface contamination of the CPR measurements. Finally, the chosen case should have intermediate reflectivity: low enough to avoid the non-Rayleigh effects in the CPR signal, but not too low since it is less sensitive than the MMCR. It is most likely that this type of situation happens a few times every year at Eureka, and since the validation needs only to be carried for some profiles to ensure a continuity in its measurements, the MMCR seems to be a viable choice.

Chapter 6
Conclusion

This project focussed on clouds and associated precipitation that passed above the ØPAL facility at Eureka in the Canadian Arctic, as observed by two cloud instruments co-located in that housing, the MMCR and AHSRL. Using two years of data, collected from September 2005 through August 2007, a first attempt to a climatology of the hydrometeors was carried out. To ensure a continuity in the results, the operational status of both instruments was checked over that two-year period, which demonstrated their reliability and self-sustained character, supporting their choice for such a long-term study in a remote location.

Synergetic retrievals have been developed, taking advantage of the strengths of each instrument. The main properties studied here were the hydrometeor coverage and phase, including the number of layers, the occurrence of precipitation, the cloud types and their combinations. When required (mostly to refine the hydrometeor phase recognition), the temperature profiles retrieved from rawinsondes launched at the Eureka's weather station were interpolated to the lidar's grid and added to the data sets. Each retrieval has been refined using a few random and extreme cases (although only one was discussed here, which was quite general). Moreover, the distinction of each atmospheric water phase received particular attention to ensure the reliability of the results, as they strongly influence the subsequent retrievals (precipitation distinction and cloud types). Thus, the assumptions about algorithm

details (such as the temperature thresholds) were verified, and it was argued that they were quite reasonable.

We observed that the hydrometeor coverage has an annual cycle similar as in other Arctic locations, maximizing in early summer and slowly decreasing through winter to minimize in spring. At Eureka, that cycle seems to come mostly from the multi-layer systems, while the single-layer clouds tend to occur about 50% of the time in every month. That cycle is also observed in the liquid (with or without solid) and high clouds occurrences, although the amplitude is different. However, the other types of clouds showed a different cycle, the low clouds almost inverting it, while the middle clouds occurrences peaked in both summer and winter. The weekly-averaged cloud boundaries also indicated an annual cycle, forming and extending higher during the summer. That cycle is most likely linked to the tropopause height (mostly the high clouds) and sunlight variations (mainly the shallow low clouds). Moreover, despite a high variability in the boundaries heights, most of the clouds stayed quite shallow (less than 1 km deep).

It was also observed that the multi-layer systems are usually consisting of different types, and generally include only two layers, one of them likely to be a low cloud. In fact, the low cloud class was the dominant one, except during the summer, when higher clouds were often experienced. The boundary layer clouds contributed the most to the low class, especially during the winter, when a temperature inversion prevented higher development and cloud top radiative cooling maintained existing stratus clouds, even showing a great variability in their coverage on a short-term basis (less than a week). The difficulty to distinguish snow falling from completely

glaciated clouds was pointed out while noticing a lack of precipitation coming from high or winter clouds. Nevertheless, it was also noticed that most of the identified precipitation did not reach the ground, especially when coming from higher levels or during summertime.

While looking into the phase of the observed hydrometeors, it was observed that solid phase hydrometeors can be found alone everywhere and at any time, although less probable in low levels during summertime, where and when the liquid is most likely to form. Furthermore, despite the great attenuation experienced by the lidar beam during the summer (causing a lot of unknown classifications), supercooled liquid was identified at temperatures lower than -20°C. In fact, it was found that those hydrometeors need more turbulence and higher relative humidity to be sustained than their solid counterparts, especially when they are mixed in the same volume.

An analysis of horizontal winds associated with different situations enlightened the role of topography and channels on the results. For instance, clear conditions were mostly found under NE winds at all levels, probably due to the presence of high mountains and non-availability of the water sources. On the contrary, cloudy conditions were found to require opposite directions aloft: single- and multi-layer clouds respectively preferred the Western and SW winds. In the low levels however, both are favoured by a South wind, while only one layer is likely to form under NW winds (both directions are following important water channels of the area, demonstrating the importance of the topography there). Moreover, those directions were also preferred by the cloudy boundary layer: the cloud is likely to extend above it

if the low-level winds are mostly from the South, while it seems to stay confined if low-level NW winds are also present, as well as NE winds aloft.

Some problems and uncertainties encountered during that project would most likely be resolved with a better differentiation of the liquid-only echoes from the mixed-phase and a classification of more hydrometeors to restrain the number of unknown, especially in summertime. Moreover, an extent of the covered time period is required to verify the reality of the results. This will be the subject of future work, as the instruments are still collecting data in Eureka. Furthermore, the possibility to extend those results to a greater area could be investigated using a similar radar/lidar synergy using the space-borne CPR and CALIOP.

Finally, we demonstrated the possibility of an Arctic validation of CloudSat's CPR measurements using Eureka's MMCR. The comparison shows a slight offset (only 1 dB) at the beginning of March 2007. It was concluded that the evaluation is possible, but only if some restrictions are respected: the case need to be homogeneous in space and time, with its hydrometeors mostly found higher than 1 km above the ground and in their solid phase, showing intermediate reflectivity factors. As the validation only needs to be completed a few times a year, this result is encouraging and could stimulate researchers to push it further and complete it, as well as to use the AHSRL to evaluate the CALIOP onboard CALIPSO, and any future space-borne cloud instruments (as the ones that will be flown by the European EarthCARE mission).

References

Ackerman, T. P. and G. M. Stokes: 2003, 'The Atmospheric Radiation Measurement program'. *Phys. Today* **56**, 38–44.

Atlas, D., S. Y. Matrosov, A. J. Heymsfield, M.-D. Chou, and D. B. Wolff: 1995, 'Radar and radiation properties of ice clouds'. *J. Appl. Meteor.* **34**, 2329–2345.

Basedi, R. J. P., J. J. M. de Wit, H. W. J. Russchenberg, J. S. Erkelens, and J. P. V. P. Baptista: 2000, 'Estimating effective radius and liquid water content from radar and lidar based on the CLARE98 data-set'. *Phys. Chem. Earth (B)* **25**(10-12), 1057–1062.

Bony, S. and J.-L. Dufresne: 2005, 'Marine boundary layer clouds at the heart of tropical cloud feedback uncertainties in climate models'. *Geophys. Res. Lett.* **32**(L20806).

CANDAC: 2008, 'Canadian Network for the Detection of Atmospheric Changes'. `www.candac.ca`.

Cess, R. D., M. H. Zhang, P. Minnis, L. Corsetti, E. G. Dutton, B. W. Forgan, D. P. Garber, W. L. Gates, J. J. Hack, E. F. Harrison, X. Jing, J. T. Kiehl, C. N. Long, J.-J. Morcette, G. L. Potter, V. Ramanathan, B. Subasilar, C. H. Withlock, D. F. Young, and Y. Zhou: 1995, 'Absorption of solar radiation by clouds: observations versus models'. *Science* **267**(5197), 496–499.

Clothiaux, E. E., T. P. Ackerman, G. G. Mace, K. P. Moran, R. T. Marchand, M. A. Miller, and B. E. Martner: 2000, 'Objective determination of cloud heights and radar reflectivities using a combination of active remote sensors at the ARM CART sites'. *J. Appl. Meteor.* **39**, 645–665.

Clothiaux, E. E., K. P. Moran, B. E. Martner, T. P. Ackerman, G. G. Mace, T. Uttal, J. H. Mather, K. B. Widener, M. A. Miller, and D. J. Rodriguez: 1999, 'The Atmospheric Radiation Measurement program cloud radars: operational modes'. *J. Atmos. Oceanic Technol.* **16**, 819–827.

Cloudnet: 2008, 'Cloudnet'. `www.cloud-net.org`.

Curry, J. A. and E. E. Ebert: 1992, 'Annual cycle of radiation fluxes over the Arctic Ocean: sensitivity to cloud optical properties'. *J. Climate* **5**, 1267–1280.

Curry, J. A., J. O. Pinto, T. Benner, and M. Tschudi: 1997, 'Evolution of the cloudy boundary layer during the autumnal freezing of the Beaufort Sea'. *J. Geophys. Res.* **102**(D12), 13851–13860.

Curry, J. A., W. B. Rossow, D. Randall, and J. L. Schramm: 1996, 'Overview of Arctic cloud and radiation characteristics'. *J. Climate* **9**, 1731–1764.

de Boer, G. and E. Eloranta: 2007, 'The University of Wisconsin Arctic high-spectral resolution lidar: general information and data examples'. In: *Second Antarctic Meteorological Observation, Modeling and Forecasting Workshop*. Rome, Italy.

Duynkerke, P. G. and J. Teixeira: 2001, 'Comparison of the ECMWF reanalysis with FIRE I observations: diurnal variation of marine stratocumulus'. *J. Climate* **14**, 1466–1478.

Eloranta, E. E.: 2005, 'High spectral resolution lidar'. In: C. Weitkamp (ed.): *Lidar: Range-Resolved Optical Remote Sensing of the Atmosphere*, Vol. 102 of *Springer Series in Optical Sciences*. New York: Springer, Chapt. 5, pp. 143–163.

Eloranta, E. W., I. A. Razenkov, J. P. Garcia, and J. Hedrick: 2004, 'Observations with the University of Wisconsin Arctic high spectral resolution lidar'. In: *22nd International Laser Radar Conference*. Matera, Italy.

Environment Canada: 2008, 'National Climate Data and Information Archive'. `www.climate.weatheroffice.ec.gc.ca`.

Frisch, A. S., C. W. Fairall, and J. B. Snider: 1995, 'Measurements of stratus cloud and drizzle parameters in ASTEX with a Ka-band Doppler radar and a microwave radiometer'. *J. Atmos. Sci.* **52**(16), 2788–2799.

Gregory, D. and D. Morris: 1996, 'The sensitivity of climate simulations to the specification of mixed phase clouds'. *Climate Dyn.* **12**, 641–651.

Gulteppe, I., G. Isaac, D. Hudak, R. Nissen, and J. W. Strapp: 2000, 'Dynamical and microphysical characteristics of Arctic clouds during BASE'. *J. Climate* **13**, 1225–1254.

Hahn, C. J., S. G. Warren, and J. London: 1995, 'The effect of moonlight on observation of cloud cover at night, and application to cloud climatology'. *J. Climate* **8**, 1429–1446.

Harrington, J. Y. and P. Q. Olsson: 2001, 'A method for the parameterization of cloud optical properties in bulk and bin microphysical models. Implications for arctic cloudy boundary layers'. *Atmos. Res.* **57**, 51–80.

Harrison, E. F., P. Minnis, B. R. Barkstrom, V. Ramanathan, R. D. Cess, and G. G. Gibson: 1990, 'Seasonal variation of cloud radiative forcing derived from the Earth Radiation Budget Experiment'. *J. Geophys. Res.* **95**(D11), 18687–18703.

Ho, C.-H., M.-D. Chou, M. Suarez, and K.-M. Lau: 1998, 'Effect of ice cloud on GCM climate simulations'. *Geophys. Res. Lett.* **25**(1), 71–74.

Hong, G.: 2007, 'Radar backscattering properties of nonspherical ice crystals at 94 GHz'. *J. Geophys. Res.* **112**(D22203).

Illingworth, A. J., R. J. Hogan, E. J. O'Connor, D. Bouniol, M. E. Brooks, J. Delanoë, D. P. Donovan, J. D. Eastment, N. Gaussiat, J. W. F. Goddard, M. Haeffelin, H. K. Baltink, O. A. Krasnov, J. Pelon, J.-M. Piriou, A. Protat, H. W. J. Russchenberg, A. Seifert, A. M. Tompkins, G.-J. van Zadelhoff, F. Vinit, U. Willén, D. R. Wilson, and C. L. Wrench: 2007, 'Cloudnet: continuous evaluation of cloud profiles in seven operational models using ground-based observations'. *Bull. Amer. Meteor. Soc.* pp. 1–16.

Intrieri, J. M., M. D. Shupe, T. Uttal, and B. J. McCarty: 2002, 'An annual cycle of Arctic cloud characteristics observed by radar and lidar at SHEBA'. *J. Geophys. Res.* **107**(C10).

Kollias, P., B. A. Albrecht, R. Lhermitte, and A. Savtchenko: 2001, 'Radar observations of updrafts, downdrafts, and turbulence in fair-weather cumuli'. *J. Atmos. Sci.* **58**, 1750–1766.

Kollias, P., G. Tselioudis, and B. A. Albrecht: 2007, 'Cloud climatology at the Southern Great Plains and the layer structure, drizzle, and atmospheric modes of continental stratus'. *J. Geophys. Res.* **112**(D09116).

Liu, Y., J. R. Key, R. A. Frey, S. A. Ackerman, and W. P. Menzel: 2004, 'Nighttime polar cloud detection with MODIS'. *Remote Sensing of Environment* **92**, 181–194.

Lubin, D. and E. Morrow: 1998, 'Evaluation of an AVHRR cloud detection and classification method over the central Arctic Ocean'. *J. Appl. Meteor.* **37**, 166–183.

Martner, B. E., D. A. Hazen, K. P. Moran, T. Uttal, M. J. Post, and W. B. Madsen: 2002, 'NOAA/ETL's vertical-profiling cloud radar and radiometer package'. In: *Sixth symposium on integrated observing system*. Seattle, WA.

Moran, K. P., B. E. Martner, M. J. Post, R. A. Kropfli, D. C. Welsh, and K. B. Widener: 1998, 'An unattended cloud-profiling radar for use in climate research'. *Bull. Amer. Meteor. Soc.* **79**(3), 443–455.

NASA Goddard Space Flight Center: 2008, 'LAADS Web: Level 1 and Atmosphere Archive and Distribution System'. `ladsweb.nascom.nasa.gov`.

Natural Resources Canada: 2007, 'The Atlas of Canada'. `atlas.nrcan.gc.ca/site/index.html`.

Piironen, P. and E. W. Eloranta: 1994, 'Demonstration of a high-spectral-resolution lidar based on an iodine absorption filter'. *Optics Lett.* **19**(3), 234–236.

Pinto, J. O.: 1998, 'Autumnal mixed-phase cloudy boundary layers in the Arctic'. *J. Atmos. Sci.* **55**, 2016–2038.

Pinto, J. O., J. A. Curry, and C. W. Fairall: 1997, 'Radiative characteristics of the Arctic atmosphere during spring as inferred from ground-based instruments'. *J. Geophys. Res.* **102**(D6), 6941–6952.

Platt, C. M. R., R. T. Austin, S. M. Sekelsky, D. L. Mitchell, and S. A. Young: 1999, 'Determining tropical cirrus particle size distributions from remote sensing with lidar, millimeter radar and infrared and microwave radiometry'. In: *9th ARM Science Team Meeting*. San Antonio, Texas.

Quante, M., H. Lemke, H. Flentje, P. Francis, and J. Pelon: 2000, 'Boundaries and internal structure of mixed-phase clouds as deduced from ground-based 95-GHz radar and airborne lidar measurements'. *Phys. Chem. Earth (B)* **25**(10-12), 889–895.

Ramanathan, V., R. D. Cess, E. F. Harrison, P. Minnis, B. R. Barkstrom, E. Ahmad, and D. Hartmann: 1989, 'Cloud-radiative forcing and climate: results from the Earth Radiation Budget Experiment'. *Science* **243**(4887), 57–63.

Randall, D., J. Curry, D. Battisti, G. Flato, R. Grumbine, S. Hakkinen, D. Martinson, R. Preller, J. Walsh, and J. Weatherly: 1998, 'Status of and outlook for large-scale modeling of atmosphere-ice-ocean interactions in the Arctic'. *Bull. Amer. Meteor. Soc.* **79**(2), 197–219.

Rangno, A. L. and P. V. Hobbs: 1991, 'Ice particle concentrations and precipitation development in small polar maritime cumuliform clouds'. *Q. J. R. Meteorol. Soc.* **117**, 207–241.

Razenkov, I. A., E. W. Eloranta, J. P. Hedrick, R. E. Holz, R. E. Kuehn, and J. P. Garcia: 2002, 'A high spectral resolution lidar designed for unattended operation in the Arctic'. In: *Proc. ILRC21*. pp. 57–60.

Rinke, A., K. Dethloff, J. H. Christensen, M. Botzet, and B. Machenhauer: 1997, 'Simulation and validation of Arctic radiation and clouds in regional climate model'. *J. Geophys. Res.* **102**(D25), 29833–29847.

Rogers, R. R. and M. K. Yau: 1989, *A short course in cloud physics*, Vol. 113 of *International Series in Natural Philosophy*. Burlington, MA: Butterworth Heinemann, 3rd edition.

Sassen, K.: 2005, 'Polarization in lidar'. In: C. Weitkamp (ed.): *Lidar: Range-Resolved Optical Remote Sensing of the Atmosphere*, Vol. 102 of *Springer series in optical sciences*. New York: Springer, Chapt. 2, pp. 19–42.

Schwartz, A. J. and T. H. V. Haar: 2008, 'A preliminary Arctic cloud climatology and radiation budget from CloudSat and CALIPSO'. In: *88th AMS annual meeting*. New Orleans, Louisiana.

Senior, C. A. and J. F. B. Mitchell: 1993, 'Carbon dioxide and climate: the impact of cloud parameterization'. *J. Climate* **6**, 393–418.

Shipley, S. T., D. H. Tracy, E. W. Eloranta, J. T. Trauger, J. T. Sroga, F. L. Roesler, and J. A. Weinman: 1983, 'High spectral resolution lidar to measure optical scattering properties of atmospheric aerosols. 1: Theory and instrumentation'. *Appl.*

Optics **22**(23), 3716–3724.

Shupe, M. D.: 2007, 'A ground-based multisensor cloud phase classifier'. *Geophys. Res. Lett.* **34**(L22809).

Shupe, M. D. and J. M. Intrieri: 2004, 'Cloud radiative forcing of the Arctic surface: the influence of cloud properties, surface albedo, and solar zenith angle'. *J. Climate* **17**, 616–628.

Shupe, M. D., P. Kollias, P. O. G. Persson, and G. M. McFarquhar: 2008a, 'Vertical motions in Arctic mixed-phase stratus'. *J. Atmos. Sci.* **65**, 1304–1322.

Shupe, M. D., P. Kollias, M. Poellot, and E. Eloranta: 2008b, 'On deriving vertical air motions from cloud radar Doppler spectra'. *J. Atmos. Oceanic Technol.* **25**, 547–557.

Shupe, M. D., S. Y. Matrosov, and T. Uttal: 2006, 'Arctic mixed-phase cloud properties derived from surface-based sensors at SHEBA'. *J. Atmos. Sci.* **63**, 697–711.

Shupe, M. D., T. Uttal, and S. Y. Matrosov: 2005, 'Arctic cloud microphysics retrievals from surface-based remote sensors at SHEBA'. *J. Appl. Meteorol.* **44**, 1544–1562.

Sokolova, E., K. Dethloff, A. Rinke, and A. Benkel: 2007, 'Planetary and synoptic scale adjustment of the Arctic atmosphere to sea ice cover changes'. *Geophys. Res. Lett.* **34**(L17816).

Stephens, G. L., D. G. Vane, R. J. Boain, G. G. Mace, K. Sassen, Z. Wang, A. J. Illingworth, E. J. O'Connor, W. B. Rossow, S. L. Durden, S. D. Miller, R. T. Austin, A. Benedetti, C. Mitrescu, and the CloudSat Science Team: 2002, 'The CloudSat mission and the A-Train: A new dimension of space-based observations of clouds and precipitation'. *Bull. Amer. Meteor. Soc.* pp. 1771–1790.

Sun, Z. and K. P. Shine: 1994, 'Studies of the radiative properties of ice and mixed-phase clouds'. *Q. J. R. Meteorol. Soc.* **120**, 111–137.

Sun, Z. and K. P. Shine: 1995, 'Parameterization of ice cloud radiative properties and its application to the potential climatic importance of mixed-phase clouds'. *J. Climate* **8**, 1874–1888.

Tinel, C., J. Testud, J. Pelon, R. J. Hogan, A. Protat, J. Delanoë, and D. Bouniol: 2005, 'The retrieval of ice-cloud properties from a cloud radar and lidar synergy'. *J. Appl. Meteor.* **44**, 860–875.

Tsushima, Y., S. Emori, T. Ogura, M. Kimoto, M. J. Webb, K. D. Williams, M. A. Ringer, B. J. Soden, B. Li, and N. Andronova: 2006, 'Importance of the mixed-phase cloud distribution in the control climate for assessing the response of clouds to carbon dioxide increase: a multi-model study'. *Climate Dyn.* **27**, 113–126.

US Department of Energy: 2008, 'Atmospheric Radiation Measurement'. `www.arm.gov`.

Uttal, T., J. A. Curry, M. G. McPhee, D. K. Perovich, R. E. Moritz, J. A. Maslanik, P. S. Guest, H. L. Stern, J. A. Moore, R. Turenne, A. Heiberg, M. C. Serreze, D. P. Wylie, O. G. Persson, C. A. Paulson, C. Halle, J. H. Morison, P. A. Wheeler, A. Makshtas, H. Welch, M. D. Shupe, J. M. Intrieri, K. Stamnes, R. W. Lindsey, R. Pinkel, W. S. Pegau, T. P. Stanton, and T. C. Grenfeld: 2002, 'Surface Heat Budget of the Arctic Ocean'. *Bull. Amer. Meteor. Soc.* pp. 255–275.

Vavrus, S.: 2004, 'The impact of cloud feedbacks on Arctic climate under greenhouse forcing'. *J. Climate* **17**, 603–615.

Verlinde, J., J. Y. Harrington, G. M. McFarquhar, V. T. Yannuzzi, A. Avramov, S. Greenberg, N. Johnson, G. Zhang, M. R. Poellot, J. H. Mather, D. D. Turner, E. W. Eloranta, B. D. Zek, A. J. Prenni, J. S. Daniel, G. L. Kok, D. C. Tobin, R. Holz, K. Sassen, D. Spangenberg, P. Minnis, T. P. Tooman, M. D. Ivey, S. J. Richardson, C. P. Bahrmann, M. Shupe, P. J. DeMott, A. J. Heymsfield, and R. Schofield: 2007, 'The Mixed-Phase Arctic Cloud Experiment'. *Bull. Amer. Meteor. Soc.* pp. 205–221.

Walsh, J. E., D. H. Portis, and W. L. Chapman: 2008, 'Use of ARM/NSA products to evaluate IPCC-AR4 Arctic cloud and radiative simulations'. In: *18th ARM Science Team Meeting*. Norfolk, Virginia.

Wandinger, U.: 2005, 'Introduction to lidar'. In: C. Weitkamp (ed.): *Lidar: Range-Resolved Optical Remote Sensing of the Atmosphere*, Vol. 102 of *Springer Series in Optical Sciences*. New York: Springer-Verlag, Chapt. 1, pp. 1–18.

Wang, X. and J. R. Key: 2003, 'Recent trends in Arctic surface, cloud, and radiation properties from space'. *Science* **299**, 1725–1728.

Wang, Z. and K. Sassen: 2002, 'Cirrus cloud microphysical property retrieval using lidar and radar measurements. Part I: Algorithm description and comparison with in situ data'. *J. Appl. Meteor.* **41**, 218–229.

Wendisch, M., P. Pilewskie, J. Pommier, S. Howard, P. Yang, A. J. Heymsfield, C. G. Schmitt, D. Baumgardner, and B. Mayer: 2005, 'Impact of cirrus crystal shape on solar spectral irradiance: a case study for subtropical cirrus'. *J. Geophys. Res.* **110**(D03202).

Winker, D. M., W. H. Hunt, and M. J. McGill: 2007, 'Initial performance assessment of CALIOP'. *Geophys. Res. Lett.* **34**(L19803).